Structure and dynamics of FCHo2 docking on membranes

F. El Alaoui[1], I. Casuso[2], D. Sanchez-Fuentes[3], C. André-Arpin[1], R. Rathar[3], V. Baecker[4], A. Castro[5], T. Lorca[5], J. Viaud[6], S. Vassilopoulos[7], A. Carretero-Genevrier[3], L. Picas[1,*].

[1]Institut de Recherche en Infectiologie de Montpellier (IRIM). CNRS UMR 9004 – Université de Montpellier, Montpellier, France.

[2]U1067 INSERM, Aix-Marseille Université, Marseille, France

[3]Institut d'Électronique et des Systèmes (IES), CNRS UMR 5214 – Université de Montpellier, Montpellier, France.

[4] Montpellier Ressources Imagerie, BioCampus Montpellier, CNRS, INSERM, University of Montpellier, 34000 Montpellier, France.

[5]Centre de Biologie Cellulaire de Montpellier (CRBM). CNRS UMR – Université de Montpellier, Montpellier, France.

[6]Institute of Metabolic and Cardiovascular Diseases (I2MC), UMR1297, Toulouse, France; University of Toulouse, Paul Sabatier University, Toulouse, France.

[7]Sorbonne Université, INSERM, Institute of Myology, Centre of Research in Myology, UMRS 974, Paris, France.

[*]Correspondence sent to: laura.picas@irim.cnrs.fr

Abstract

Clathrin-mediated endocytosis is a paradigm of a cellular processes that is orchestrated by phosphoinositides, where the plasma membrane phosphatidylinositol-4,5-bisphosphate (PI(4,5)P_2) plays an instrumental role in the formation of clathrin-coated structures. Among the early endocytic proteins that

reach at the plasma membrane, the F-BAR domain only protein 1 and 2 complex (FCHo1/2) is thought to orchestrate the early stages but, the exact mechanism triggering its nucleation on membranes is not well understood. By combining bottom-up synthetic approaches on *in vitro* and cellular membranes, we show the molecular dynamics of FCHo2 self-assembly on membranes. Our results indicate that PI(4,5)P_2 guide the recruitment of FCHo2 at specific regions of the membrane, where it self-assembles into ring-like shape protein patches flanked by membrane invaginations. Importantly, we show that binding of FCHo2 on cellular membranes promotes the enrichment of PI(4,5)P_2 at the boundary of specific cargo receptors, such as the epidermal growth factor receptor (EGFR). Thus, our results provide a mechanistic framework that could explain the orchestration of early PI(4,5)P_2-interacting proteins recruitment at endocytic sites.

Introduction

Phosphoinositides are essential lipids in multiple cellular processes by providing docking sites for key proteins involved in cell adhesion, migration and membrane trafficking or as precursors of secondary messengers(*1*, *2*). Clathrin-mediated endocytosis (CME) is a key trafficking pathway in eukaryotic cells that is orchestrated by the metabolic conversion of phosphoinositides at the plasma membrane(*3*, *4*). The biogenesis of clathrin-coated vesicles requires a precise and coordinated recruitment of more than ~ 50 different proteins at the plasma membrane to achieve the bending, elongation and fission steps(*5*, *6*). Although the initiation of endocytosis is a critical step, the exact mechanisms triggering the nucleation of endocytic proteins at the plasma membrane is not well understood. The early stages of CME entail the nucleation of adaptor and accessory proteins, cargo and lipids to undergo the bending of the plasma membrane(*7*). Several studies have shown that FCHo1/2 (Fer/CIP4 homology domain only protein 1 or 2) is among the early proteins recruited at endocytic sites(*5*, *8*), where it is thought to establish a network of interactions with pioneer proteins, such as EPS15, Intersectin adaptor protein 2 (AP2), and transmembrane cargo(*5*, *9*, *10*). FCHo paralogs associate with membranes through the dimerization of F-BAR domains displaying a shallow concave surface that interacts with acidic phospholipids(*8*, *11*, *12*). The F-BAR scaffold is followed by a polybasic motif, which provides a selective recognition for the plasma membrane PI(4,5)P_2(*8*). To date, how FCHo1/2 is recruited to membranes is still an open question. In CME, the plasma membrane pool of PI(4,5)P_2 is essential to initiate protein assembly, whereas local PI(4,5)P_2 conversion controls the progression to latter stages in the maturation of clathrin-coated vesicles(*3*, *4*, *13*). Interestingly, several endocytic proteins, including the F-BAR domain of the yeast homolog of FCHo1/2, have been reported to assist the reorganization of PI(4,5)P_2 molecules on *in vitro* systems(*14*, *15*). Also, the FCHo1/2 effector AP2 was shown to create a local pool of PI(4,5)P_2 by stimulating the metabolic activity

of dedicated kinases(*16*), although it requires PI(4,5)P_2 for its localization and activation at the plasma membrane(*17*, *18*). Finally, electrostatic interactions through polybasic motifs at the cytoplasmic tail of transmembrane cargoes were shown to be associated with PI(4,5)P_2-enriched domains, as in the case for the epidermal growth factor receptor (EGFR)(*19–21*). However, the exact role of the nanoscale organization of phosphoinositides during the initiation of CME is yet to be determined.

Here we combined sub-diffraction microscopy and high-speed atomic force microscopy with *in vitro* and *in cellulo* systems to show that PI(4,5)P_2 domains spatially and temporally regulate the nucleation of FCHo2 on flat membranes through the self-assembly of diffusion-mediated ring-like shaped protein patches. Our results indicate that, in the absence of metabolizing enzymes, FCHo2 is able to engage a local PI(4,5)P_2 enrichment at the boundaries of the transmembrane cargoes holding a polybasic sequence at the cytoplasmic tail, such as the EGFR. By using a lithographic approach to manipulate membrane curvature, we found that the interaction with PI(4,5)P_2 supports the partition of FCHo2 at the edges of dome-like structures. Collectively, our work points out to PI(4,5)P_2 lateral lipid heterogeneities as an organizing mechanism supporting the nucleation and self-organization of PI(4,5)P_2-interacting proteins during the initial stages of CME.

Results

PI(4,5)P_2 domains regulate the binding and self-organization of FCHo2 on flat membranes

Like many endocytic proteins, FCHo1/2 was previously reported to interact with PI(4,5)P_2 through a polybasic region that is located downstream of its F-BAR domain (*8*). To study how FCHo1/2 is recruited on membranes, we monitored by airyscan microscopy the binding of recombinant full-length FCHo2-Alexa647 on supported lipid bilayers containing 20% of negatively charged lipids and increased % mol of PI(4,5)P_2 at the expenses of phosphatidylserine (PS). We determined the functionality of FCHo2 by performing a tubulation assay using membrane sheets made of brain polar lipids, as previously reported(*22*) (Figure S1). To monitor the local enrichment of PI(4,5)P_2 we doped supported lipid bilayers with 0.2% mol of fluorescent PI(4,5)P2 (TF-TMR- PI(4,5)P_2) and 0.2% of Oregon Green 488 1,2-Dihexadecanoyl-sn-Glycero-3-Phosphoethanolamine (OG-DHPE) at the expenses of their non-labeled counterpart (Figure 1A). The resulting supported lipid bilayers displayed an homogeneous membrane distribution of lipids, as denoted by the equivalent partitioning of the signal corresponding to the fluorescent DHPE and PI(4,5)P_2 dyes all over the membrane (Figure 1A, homogenous). We could identify the existence of PI(4,5)P_2-enriched regions, which appear as discrete spots that display a local increase in TF-TMR- PI(4,5)P_2 that is accompanied by a decrease in the intensity of OG-DHPE co-localizing with FCHo2 molecular clusters

(Figure 1A, domain). As a result, PI(4,5)P_2-enriched regions can be differentiated from residual adhered vesicles (diameter ~ 100 nm) or membrane defects as they display an equivalent increase in the intensity of both lipid dyes (Figure 1A, vesicle). The observation of FCHo2 molecular clusters is in agreement with previous electron microscopy studies predicting the organization of F-BAR domain proteins into small aggregates on flat membranes(*11*). To understand the contribution of the surface availability of PI(4,5)P_2 on the formation of FCHo2 molecular clusters, we estimated the binding of the protein as a function of the PI(4,5)P_2 enrichment (% mol, Figure 1B). We observed that increasing amounts of PI(4,5)P_2 favored FCHo2 binding on flat membranes. However, an increase in the % mole of PI(4,5)P_2 did not affect the apparent size of FCHo2 clusters (median value ~ 0.07 μm^2, Figure 1C).

To established the dynamics of FCHo2 association with membranes containing 5% of PI(4,5)P_2, we performed a temporal analysis (Figure 1D and E) and observed that FCHo2 binding to PI(4,5)P_2-enriched domains resulted in the formation of long-lived molecular clusters (red arrow, Figure 1E), whereas its association with an homogenous distribution of PI(4,5)P_2 was more likely to lead to cluster disassembly (gray arrow, Figure 1E). Under these experimental conditions we could not detect a local segregation of PI(4,5)P_2 molecules upon binding of FCHo2 on supported lipid bilayers. Next, to determine the contribution of the F-BAR domain in the organization of the full-length protein into molecular clusters, we analyzed the interaction of F-BAR-Alexa647 with flat membranes at different % mol of PI(4,5)P_2 (Figure 1F and S2). Our results show that the binding of the F-BAR domain is enhanced at 5 % mol of PI(4,5)P_2, where it assembles into sub-micrometric molecular clusters with a median dimension that was moderately larger than in the case of the full-length protein, i.e. ~ 0.09 μm^2 (Figure 1G). Thus, we hypothesized that these differences in size could arise as a result of the selective interaction of the PI(4,5)P_2-interacting motif of FCHo2. Indeed, we found a positive correlation between the signal of FCHo2 and the size of PI(4,5)P_2 domains, which was larger than in the case of the F-BAR domain alone. We compared our observations with the surface organization of the GFP-PH domain of PLCδ1 (PH(PLCδ1)), which presents a stereospecific recognition for PI(4,5)P_2(*3*) and found a similar surface organization to that observed for FCHo2, which was characterized by the formation of a protein layer and the occurrence of small spots with a median dimension of ~ 0.07 μm^2. This was also the case with the FBP17 (Toca-2), another PI(4,5)P_2-binding F-BAR domain containing protein(*22*) (Figure S3). Collectively, these observations indicate that PI(4,5)P_2-enriched domains assist the spatial and temporal self-assembly of FCHo2 into molecular clusters, a process that is assisted by the ability of F-BAR domain proteins to polymerize.

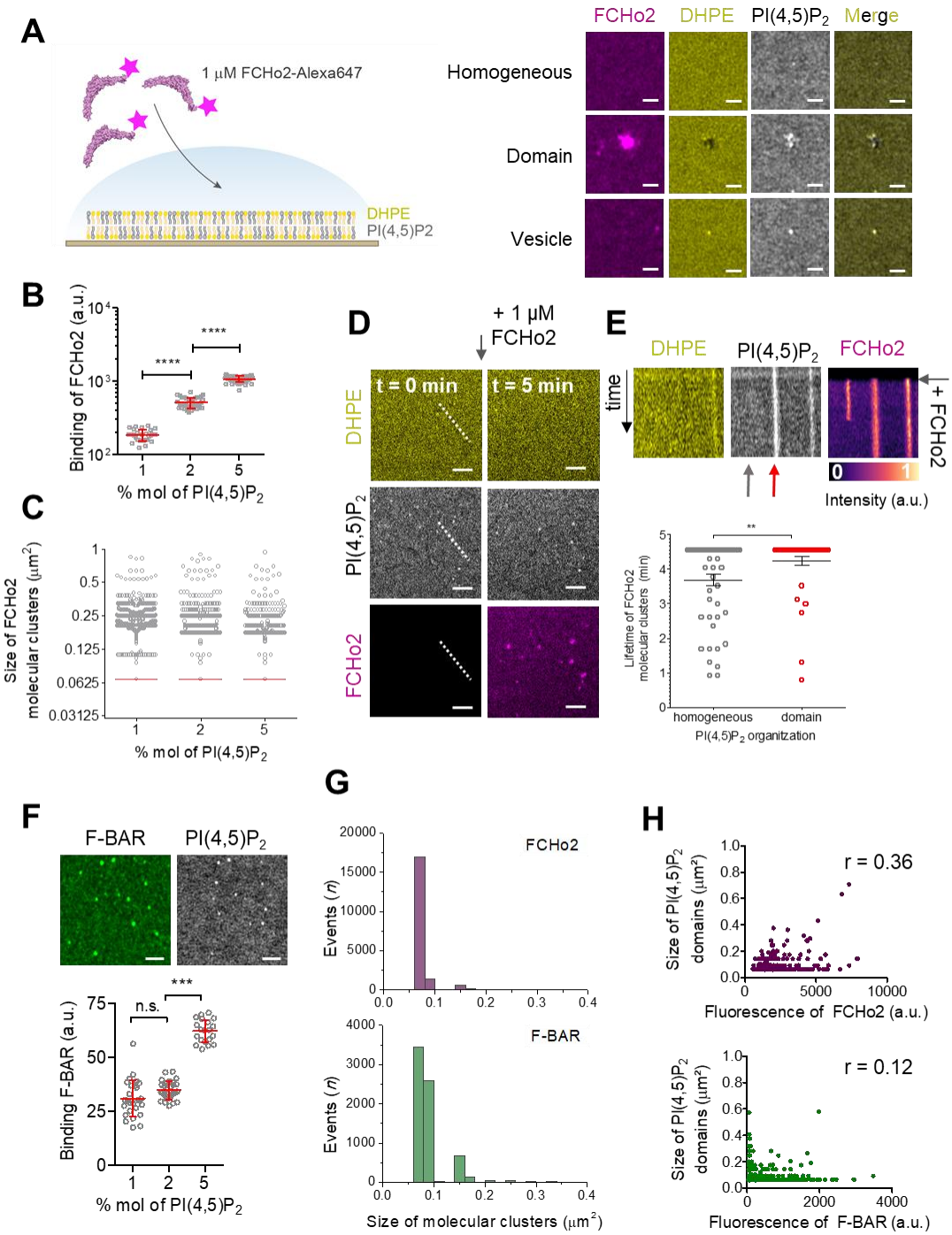
A
1 μM FCHo2-Alexa647
DHPE
PI(4,5)P2
FCHo2
DHPE
PI(4,5)P2
Merge
Homogeneous
Domain
Vesicle
B
Binding of FCHo2 (a.u.)
% mol of PI(4,5)P2
C
Size of FCHo2 molecular clusters (μm2)
% mol of PI(4,5)P2
D
+ 1 μM FCHo2
t = 0 min
t = 5 min
DHPE
PI(4,5)P2
FCHo2
E
DHPE
PI(4,5)P2
FCHo2
time
+ FCHo2
Intensity (a.u.)
Lifetime of FCHo2 molecular clusters (min)
homogeneous
domain
PI(4,5)P2 organization
F
F-BAR
PI(4,5)P2
n.s.
Binding F-BAR (a.u.)
% mol of PI(4,5)P2
G
FCHo2
F-BAR
Events (n)
Size of molecular clusters (μm2)
H
r = 0.36
Size of PI(4,5)P2 domains (μm2)
Fluorescence of FCHo2 (a.u.)
r = 0.12
Size of PI(4,5)P2 domains (μm2)
Fluorescence of F-BAR (a.u.)

Figure 1. **FCHo2 self-assembly into molecular clusters is assisted by the surface organization of PI(4,5)P_2.** (A) *Left*, cartoon of the experimental setup to detect the interaction of FCHo2-A647 with PI(4,5)P_2-enriched domains. *Right*, representative airyscan images showing the main types of protein and lipid organizations that were detected under the experimental conditions: (i) an homogenous FCHo2 and PI(4,5)P_2 organization, (ii) the formation of protein and lipid domains and (iii) the presence of non-fused lipid vesicles. Scale bar, 1 µm. (B) Binding of FCHo2 on membranes containing different % mol of PI(4,5)P_2, at the expenses of 20% of total negative charge. Mean ± s.d. is displayed in red and one-way ANOVA in black. n=31, n=39, and n=54 for 1%, 2%, and 5% mol of PI(4,5)P_2 respectively. (C) Size distribution of FCHo2 molecular clusters (in µm²) on membranes containing % mol of PI(4,5)P_2. Median value is displayed in red. n=63949, n=16631, and n=19287 for 1%, 2%, and 5% mol of PI(4,5)P_2, respectively. (D) Airyscan time-lapse showing the dynamics of FCHo2 association with membranes containing 5% of PI(4,5)P_2 upon addition of 1 µM of FCHo2-A647. Scale bar, 2 µm. (E) *Top*, representative kymograph along the white dashed line in D. Time scale is 5 min. Size is 11 µm. *Bottom*, lifetime of FCHo2 molecular clusters (in min) relative to the PI(4,5)P_2 organization: homogeneous (grey) or on domains (red) as highlighted by the arrows in the corresponding kymograph image. Mean ± s.d. and one-way ANOVA are displayed in black. n=50, n=43 for an homogeneous an on domains PI(4,5)P_2 organization, respectively. (F) *Top*, representative airyscan images showing the organization of F-BAR-A647 domain association with membranes containing 5% of PI(4,5)P_2. Scale bar, 2 µm. *Bottom*, binding of F-BAR on membranes containing different % mol of PI(4,5)P_2. Mean ± s.d. is displayed in red and one-way ANOVA in black. n=27, n=29, and n=20 for 1%, 2%, and 5% mol of PI(4,5)P_2 respectively. (G) Distribution of the size of molecular clusters of FCHo2 (purple) and F-BAR (green) on PI(4,5)P_2-containing membranes. (H) Scatter plots of the correlation between the intensity of FCHo2 (purple) and F-BAR (green) relative to the size of PI(4,5)P_2-enriched domains on 5% mol PI(4,5)P_2-containing membranes. n=11448 for FCHo2 and n=12828 for F-BAR. The correlation coefficient, r, was r = 0.36 and r = 0.12, respectively.

FCHo2 diffusion drives the formation and growth of ring-like protein patches

To investigate FCHo2 cluster biogenesis on PI(4,5)P_2-containing membranes at the molecular level, we used high-speed atomic force microscopy (HS-AFM). Supported lipid bilayers doped with 5% PI(4,5)P_2 were formed on freshly cleaved mica disks (see methods section). Homogeneity and absence of defects of supported bilayers under the imaging buffer were confirmed before the addition of proteins. Injection of full-length FCHo2 at 1 µM in the HS-AFM imaging chamber resulted in the formation of sub-micrometric protein patches with a median dimension of ~ 0.005 μm^2 that protruded out of the flat membrane surface with an average height of ~ 47 ± 3 nm (Figure 2A-C). Increase in the setpoint force from minimal values (a few tens of pN) to intense forces (around one hundred pN) resulted in the reduction of the height of FCHo2 clusters down to ~ 15 ± 2 nm, suggesting that FCHo2 is able to moderately bend supported lipid membranes at minimal AFM imaging forces.

Real time imaging of the initial stages revealed the entire molecular process of FCHo2 cluster formation, from the binding of single FCHo2 homodimers to the growth of molecular clusters (Figure 2D). Representative time-lapse images and kymograph analysis along the dashed region at t = 0 s showed that

the binding of individual FCHo2 proteins engages an indentation of few nm in the lipid membrane adjacent to the protein surface (Figure 2E, green arrowheads), which could be delineated from the cross-section profile along the red dashed box of the kymograph (Figure 2D). Binding of FCHo2 is rapidly convoyed by the arrival of additional FCHo2 homodimers (as highlighted by white arrowheads in the kymograph). This stage of the process was characterized by minimal lateral interactions and the existence of contacts between the tails of full-length FCHo2 dimers and that we designated as tail-to-tail interactions, ultimately leading to a ring-like organization (Figure 2F). This dynamic reorganization that we named as the "ring formation" step (Figure 2D), spanned over ~ 80-100 s.

The identification of individual proteins at these initial stages allowed us to extract the average distance between the two extremities of the full length protein, denoted as FCHo2 tail-to-tail distance, which was of ~ 32 ± 8 nm (Figure 2G) and in good agreement with the size of the F-BAR domain estimated from electron microscopy micrographs to be ~ 22 nm(*11*). After this stage, FCHo2 clusters start to enlarge as a result of the diffusion of FCHo2 homodimers and tail-to-tail docking to the initial FCHo2 ring-like structure (Figure 2D, white arrowheads). During the cluster growth stage, we found that FCHo2 self-organizes into hollow ring-like assemblies, a structural pattern that was particularly discernible at the growth front of FCHo2 molecular clusters (Figure 1H and magnified image). We estimated the tail-to-tail docking time of individual proteins during the expansion of the cluster to be of ~ 115 ± 94 s (Figure 2I). Collectively, our results suggest that the end-to-end addition of homodimers to the initial protein ring-like shape organization is likely to confer structural stability allowing anisotropic growth and the formation of molecular clusters, a process that reached its equilibrium in the time-scale of minutes (Figure 1 and Figure 2H).

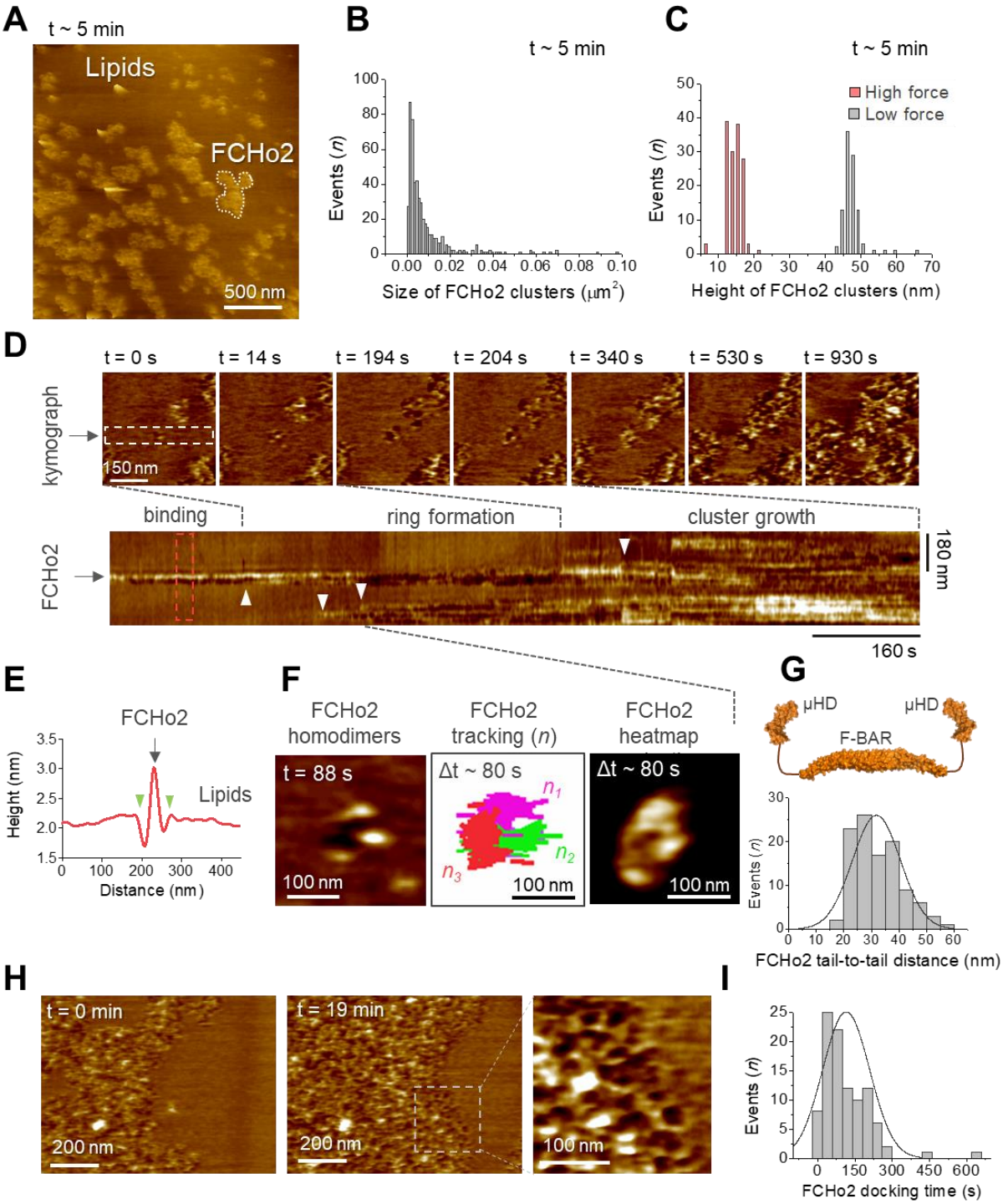

Figure 2. Molecular dynamics of FCHo2 self-assembly on PI(4,5)P_2-containing membranes. (A) Representative large scan HS-AFM image of FCHo2 molecular clusters (white dashed region) on supported lipid bilayers containing 5% mol PI(4,5)P_2 at t ≥ 5 min. (B) Distribution of the size of FCHo2 molecular clusters (in μm²) obtained from HS-AFM images at t ≥ 5 min. (C) Distribution of the height of FCHo2 molecular clusters (in nm) at low (gray) and high (red) setpoint forces at t ≥ 5 min. (D) HS-AFM movie frames of the binding of FCHo2 on 5% mol PI(4,5)P_2-containing membranes. Kymograph analysis performed on the

white outline to display the representative stages of FCHo2 binding and self-assembly on flat membranes. White arrowheads highlight the docking of new FCHo2 homodimers to the growing molecular cluster. (E) Profile analysis along the red outline in D. Green arrowheads highlight the membrane indentation upon binding of FCHo2 on lipid membranes. (F) HS-AFM movie snapshot of the FCHo2 ring formation along with a representative tracking of individual homodimers (n = 3) and the heat map projection within a time frame, Δt, of ~ 80 s. (G) Distribution of the tail-to-tail distance (in nm) estimated from individual FCHo2 proteins before the cluster growth ($t \leq$ 100-200 s) and schematics of the FCHo2 tail-to-tail structure from the PDB 2V0O (F-BAR) and 5JP2 (μHD) entries (H) Representative HS-AFM snapshots (t = 0 min and t = 19 min) illustrating the growth of FCHo2 molecular clusters into ring-like shape protein patches. Magnified image corresponds to the dashed outline. (I) Distribution of the end-to-end docking time (in s) during the growth of FCHo2 clusters.

Cytosolic components promote the reorganization of FCHo2 on membranes

The fact that a fraction of FCHo2 forms a protein layer on PI(4,5)P_2-containing in membranes (Figure 1A) suggests that this pool of the protein could be accessible for the formation of new molecular clusters and/or buffer the growth of those already present on membranes. To test this hypothesis, we produced the active cytosolic components, including endogenous FCHo2, triggering clathrin-coat assembly by using *Xenopus* egg extracts, a method that is well-reported to reconstitute complex cellular processes such as endocytosis(*23*, *24*). Extracts were supplemented with a freshly prepared "energy mix", as previously reported(*25*). First we determined by immunofluorescence the ability of the cytosolic extracts to trigger the formation of Clathrin-positive events on supported lipid bilayers containing 5% mol PI(4,5)P_2 that were previously incubated with 1 μM of FCHo2-Alexa647. As expected, the addition of 4 mg·ml^{-1} of cytosolic extracts lead to the reorganization of the PI(4,5)P_2 and the identification of puncta that were positive for both FCHo2 and the Clathrin antibody, as compared to the energy mix alone (Figure 3A-B and Figure S4). Next, we analyzed the dynamics of FCHo2 under the same experimental conditions. Injection of cytosolic extracts into the imaging chamber resulted in the immediate reorganization of the FCHo2 protein layer into molecular clusters (Figure 3C and D). This dynamic effect was also observed in the presence of the energy mix alone, although to a lesser extent (Figure S6). Indeed, in the presence of cytosolic extracts we observed a 2-fold increase in the area fraction of newly formed molecular clusters, as compared to the energy mix (Figure 3E). The evolution of the fluorescence intensity against time of FCHo2, DHPE and PI(4,5)P_2 showed that at time scales < 6 min, the reorganization of FCHo2 into molecular clusters was not associated with a local enrichment of PI(4,5)P_2 molecules (Figure 3D). In agreement with our previous observations (Figure 1D), we detected the disassembly of newly formed FCHo2 clusters in the absence of PI(4,5)P_2-enriched domains (Figure 3C-D and Figure S5). The estimation of the average size of FCHo2 molecular clusters in the presence of cytosolic extracts showed a 1.5-fold increase in the sub-micrometric mean dimension of protein patches, as compared to control conditions or the energy mix alone (Figure 1C and

Figure 3F, respectively). Altogether, these results point out that the membrane-bound FCHo2 protein layer is functional and thus, that it is able to reversibly separate into protein assemblies in the presence of active cytosolic extracts.

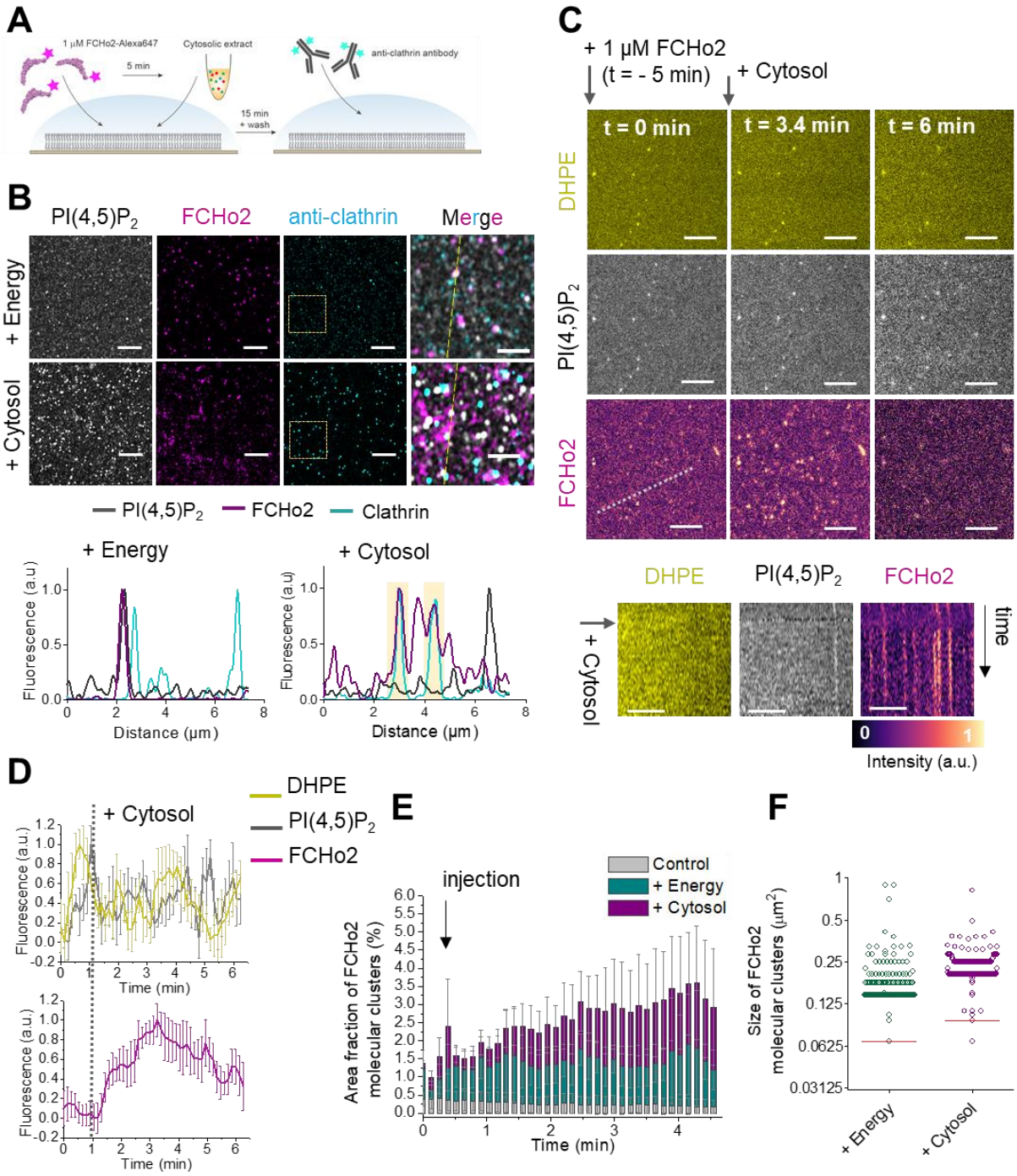

Figure 3. **The FCHo2 protein layer is reorganized in the presence of cytosolic extracts**. (A) Cartoon of the immunofluorescence assay to detect FCHo2-Alexa647 positive for clathrin on 5% mol PI(4,5)P_2-containing supported lipid bilayers incubated with 4

mg/ml of cytosolic extract and/or the energy mix. *Bottom*, representative airyscan images of the immunofluorescence assay showing the localization of PI(4,5)P_2 (gray), FCHo2 (magenta) and clathrin (cyan, anti-clathrin antibody) on membranes incubated with the energy mix alone (+ Energy) or with cytosolic extract and energy mix (+ Cytosol). Sale bar, 5 µm. (B) Airyscan time-lapse showing the membrane reorganization of DHPE (yellow), PI(4,5)P_2 (grey) and FCHo2 (magenta) after injection of the cytosolic extract and energy mix (+ Cytosol). (C) *Top*, kymograph analysis along the dashed line in B. Time scale is 6 min. Scale bar, 5 µm. *Bottom*, Fluorescence quantification over time of DHPE (yellow), PI(4,5)P_2 (grey) and FCHo2 (magenta) upon addition of the cytosolic extract and energy mix (+ Cytosol). Each curve represents the mean ± s.d., n = 7. (D) Distribution of the % area fraction of FCHo2 molecular clusters after injection of buffer (Control, gray), the energy mix alone (+ Energy, green) or with cytosolic extract and energy mix (+ Cytosol, magenta) over time (t = 5 min). (E) Size of FCHo2 molecular clusters (in µm²) on 5% mol PI(4,5)P_2-containing membranes in presence (magenta) or absence of cytosolic extracts (green). Median value is displayed in red. n=1804, n=13716 for the + Energy and + Cytosol condition, respectively.

FCHo2-mediated PI(4,5)P_2 enrichment is cargo receptor specific

Because FCHo2 molecular clusters are preferentially formed on PI(4,5)P_2-enriched domains (Figure 1) that accumulate Clathrin (Figure 3), we wondered if their nucleation on cellular membranes could be mediated by Clathrin-regulated cargo receptors (*8*, *26*). Interestingly, the EGF receptor (EGFR) was reported to interact with PI(4,5)P_2-enriched domains through a polybasic motif at the cytoplasmic region(*20*, *21*, *27*). Although it is unclear whether cargo can initiate its own endocytosis(*7*), it might be possible that the association of EGFRs with PI(4,5)P_2 nanodomains could assist accumulation of FCHo2 on cellular membranes. Accordingly, we monitored FCHo2-Alexa647 recruitment dynamics on plasma membrane sheets that were obtained by ultrasound-mediated unroofing of cells stably expressing EGFR-GFP and subsequently doped with 0.2% mol of fluorescent PI(4,5)P_2 (TF-TMR- PI(4,5)P_2) (Figure 4A). To prevent receptor clustering, we generated a stable HT1080 cell line expressing EGFR-GFP displaying a homogenous surface expression and background receptor activation in the absence of EGF (Figure S6). Injection of 1 µM FCHo2-Alexa647 on EGFR-GFP plasma membrane sheets lead to the binding of the protein and the formation of sub-micrometric FCHo2 molecular clusters (Figure 4B-C), which displayed a median dimension of ~ 0.07 μm^2, in agreement with our observations in supported lipid bilayers (Figure S7). As expected, we detected a population of EGFR-GFP spots that co-localized with PI(4,5)P_2-enriched domains, although the majority of the receptor displayed an homogenous partitioning on plasma membrane sheets (Figure 4B and Figure S8). Kymograph analysis on these sheets showed that binding of FCHo2 is accompanied by a local increase in the PI(4,5)P_2 signal at the boundaries of EGFR-GFP-positive spots. The FCHo2-mediated PI(4,5)P_2 reorganization also induced a concomitant increase in the EGFR-GFP signal, possibly indicating a positive feedback mechanism as result of the PI(4,5)P_2 accumulation. This behavior was independent of the initial surface organization of the EGFR previous to the addition of FCHo2 (i.e.

homogeneous or associated to PI(4,5)P_2-positive spots) (Figure 4C-D and Figure S9). Conversely, in the absence of EGFR spot formation we did not detect a local PI(4,5)P_2 enrichment upon binding of FCHo2. Thus, suggesting that although PI(4,5)P_2 reorganization is likely to be triggered by FCHo2, the clustering of the EGFR is required to support its local accumulation possibly through to the presence of a polybasic PI(4,5)P_2-interacting region at the cytoplasmic tail. PI(4,5)P_2 depletion and EGFR mutagenesis at the cytoplasmic tail were shown to impair receptor clustering(*21*). Thus, to confirm our hypothesis, we monitored the binding of FCHo2-Alexa647 in the presence of the transferrin receptor (TfR), another clathrin-regulated cargo which has not been reported to interact with PI(4,5)P_2. To this end, we generated transferrin receptor (TfR)-GFP plasma membrane sheets (Figure 4E-F and Figure S10). Analysis of the dynamics of FCHo2 recruitment on either TfR-positive spots or in the absence of TfR accumulation showed that binding of the protein did not engage a major reorganization of the PI(4,5)P_2 signal, as compared with the trend observed on EGFR-positive spots (Figure 4F-G). Thus, our results suggest that FCHo2-mediated PI(4,5)P_2 accumulation on cellular membranes is specific to the structural characteristics of each cargo receptor.

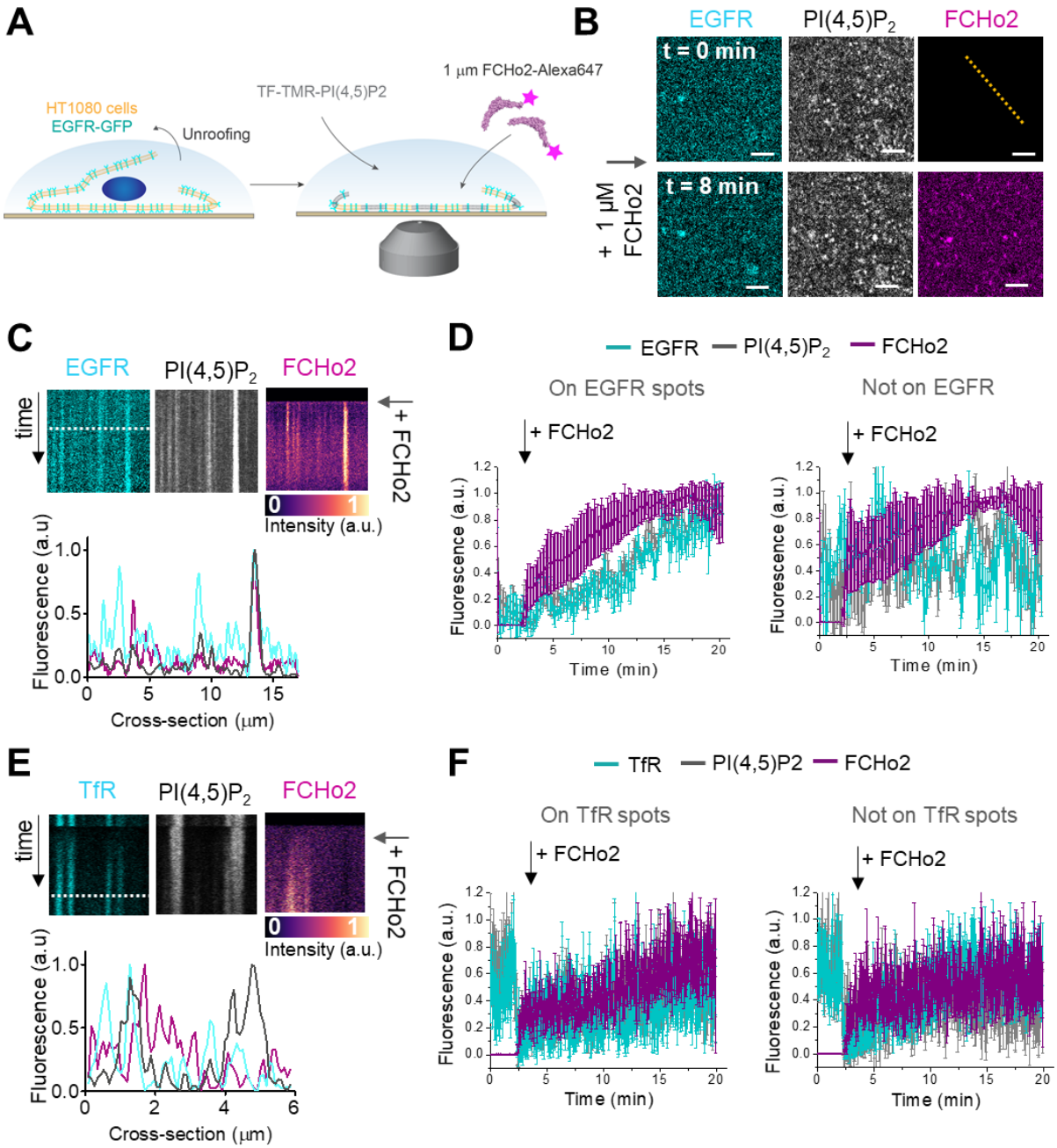

Figure 4. **FCHo2 assembles into molecular clusters on cellular membranes.** (A) Cartoon of the experimental setup to monitor the recruitment of FCHo2-Alexa647 on cellular membranes obtained by unroofing of HT-1080 cells expressing EGFR-GFP and doped with fluorescent PI(4,5)P_2. (B) Representative airyscan time-lapse images showing the dynamics of PI(4,5)P_2 (gray), FCHo2 (magenta) and EGFR-GFP (cyan) on plasma membrane sheets. Scale bar, 5 µm. (C) *Top*, kymograph analysis along the dashed line in B. Time scale is 20 min. Size is 17 µm. *Bottom*, intensity profile of the EGFR (cyan), PI(4,5)P_2 (gray) and FCHo2 (magenta) along the dashed line in the kymograph. (D) Fluorescence quantification over time of the EGFR (cyan), PI(4,5)P_2 (grey) upon injection of 1µm of FCHo2-Alexa647 (magenta) relative to the formation or not of EGFR spots positive for FCHo2 on plasma

membrane sheets. Each curve represents the mean ± s.d., n ≥ 5. (E) *Top*, kymograph analysis of the dynamics of PI(4,5)P_2 (gray), FCHo2 (magenta) and TfR-GFP (cyan) on plasma membrane sheets. Time scale is 20 min. Size is 6 µm. *Bottom*, intensity profile of the TfR (cyan), PI(4,5)P_2 (gray) and FCHo2 (magenta) along the dashed line in the kymograph. (D) Fluorescence quantification over time of the TfR (cyan), PI(4,5)P_2 (grey) upon injection of 1µm of FCHo2-Alexa647 (magenta) relative to the formation or not of TfR spots positive for FCHo2 on plasma membrane sheets. Each curve represents the mean ± s.d., n = 6.

PI(4,5)P_2 interaction assists the partitioning of FCHo2 on curved membranes

The observation that FCHo2 organizes into ring-like shaped protein patches is a diffusion-driven process (Figure 2) suggests that membrane curvature is likely to affect the assembly process, as curvature is known to affect protein diffusion(*28*). Indeed, membrane curvature plays a pivotal role in CME, where the transition from a flat surface to a dome-like invagination is a required step for the biogenesis of clathrin-coated vesicles(*6*). To monitor the organization of FCHo2 as a function of membrane shape, we engineered arrays of SiO_2 vertical nanostructures of different radii, *R*, using soft nano-imprint lithography (soft-NIL) (Figure S11), as previously reported(*29*). SiO_2 nanopatterned substrates were thereafter functionalized with supported lipid bilayers containing 20% of negatively charged lipids. First, we determined by airyscan microscopy the surface organization of the F-BAR domain and full-length FCHo2 labeled with Alexa647 on nano-domes of R ~ 150 nm (Figure 5A) that were previously functionalized with lipid membranes containing 5% mol PI(4,5)P_2. The three-dimensional (3D) rendering of the protein signals relative to the DHPE lipid dye, which depict the pillar dimension, showed that while the F-BAR domain preferentially accumulates at the base of the dome, the FCHo2 staining expanded all over the surface of the structure but without reaching its upper region (Figure 5B). This unexpected result led us to hypothesize that selective interaction of FCHo2 with PI(4,5)P_2 could play a role in its different organization with respect to the F-BAR domain alone. Consequently, we replaced the 5% mol of PI(4,5)P_2 by PS (20% mol PS), which was traduced in the binding of FCHo2 along the entire nano-dome surface (Figure 5B, yellow). To quantitatively determine the existence of a preferential localization of proteins as a function of the lipid composition, we computed for each nano-dome of the nanopatterned array the normalized maximal height of the protein signal relative to the DHPE lipid signal, which was used as a reference of the nano-dome height (see methods). Thus, a normalized maximal height close to ~ 1.0 would indicate an increased probability of detecting the protein at the top of the nanostructure, whereas a value of ~ 0 would reflect a preferential localization at the base. In the case of the F-BAR domain, we obtained a median value of its maximal height ~ 0 on nano-domes of R ~ 150 nm (Figure 5C, green). For the full-length protein we detected two preferential localizations, at the base and at the mid of the nano-dome, although the median height obtained was of ~ 0.64 in the presence of PI(4,5)P_2-containing membranes (Figure 5C, magenta). In agreement with

the 3D renderings, on membranes exclusively containing PS we obtained that the median maximal height of FCHo2 was of ~ 1 (Figure 5C, yellow), thus pointing out that FCHo2 assembly on curved membranes is likely to be modulated by the interaction with the acidic lipid environment. To test this hypothesis we monitored the binding of another full-length F-BAR domain protein, FBP17-Alexa647, which similarly to FCHo2 also has an enhanced interaction with negatively charged membranes containing PI(4,5)P_2(*22*). We found that on nano-domes of R ~ 150 nm, FBP17 localization was not exclusively restricted to the base of the dome (Figure 5D), as observed in the case of the F-BAR domain alone (Figure 5B). Next, we asked if FCHo2 patterning on nano-domes might arise from an heterogeneous distribution of PI(4,5)P_2 on vertical nanostructures. To this end, we estimated the axial localization of fluorescent PI(4,5)P_2 relative to the DHPE lipid dye (Figure 5E). Under our experimental conditions we could not detect differences in the surface organization of both the DHPE and PI(4,5)P_2 lipid dyes, thus suggesting that they are likely to display an homogenous organization. This feature was independent of the dimension of the vertical nanostructures that we tested (Figure S12). To confirm that TF-TMR-PI(4,5)P_2 signal was replicating the actual organization of the total pool of PI(4,5)P_2 on nano-domes we monitored the signal of a selective PI(4,5)P_2-binding domain, the PH(PLCδ1), on 5% PI(4,5)P_2-containing bilayers (Figure 5F). The resulting median of the maximal height of PH(PLCδ1) was ~ 1.0, independently of the size of the vertical nanostructure (Figure S13), indicating that indeed PI(4,5)P_2 is likely to display an homogenous distribution on SiO_2 nanostructures. Thus, suggesting that the partitioning of FCHo2 on nano-domes might not be due to the existence of PI(4,5)P_2 heterogeneities but instead, might reflect the effect that membrane curvature has on protein diffusion and consequently, on the assembly of FCHo2 into molecular clusters. Because the effect of membrane curvature on protein diffusion was shown to be inversely proportional to the radius of curvature(*28*), we increased the dimension of PI(4,5)P_2-functionalized vertical nanostructures from domes of R ~ 150 nm to pillars of R ~ 300 nm (Figure 5G). As a result, the use of larger circle diameters to which F-BAR proteins typically associate(*30*) should reveal the impact of the lateral mobility on FCHo2 assembly, rather than the scaffolding capabilities of the banana-shaped F-BAR domain. The estimation of the normalized maximal height of FCHo2 showed a median value of ~ 0.8 and 0.9 on structures of R ~ 200 and 300 nm, respectively (Figure 5H), pointing out that the increase on the nanostructure radius increases the probability to detect FCHo2 along the entire nanostructure. This trend was also observed in the case of the F-BAR domain alone with a median value of its maximal height localization of ~ 0.7 and 0.8 on structures of R ~ 200 and 300 nm, respectively (Figure 5H), although we could also detect that part of the protein was still binding at the base of nanostructures. Collectively, these observations point out that PI(4,5)P_2-interaction assist the partitioning FCHo2 on domes of radii ≤ 150 nm, possibly as a result of the reduction in protein diffusion.

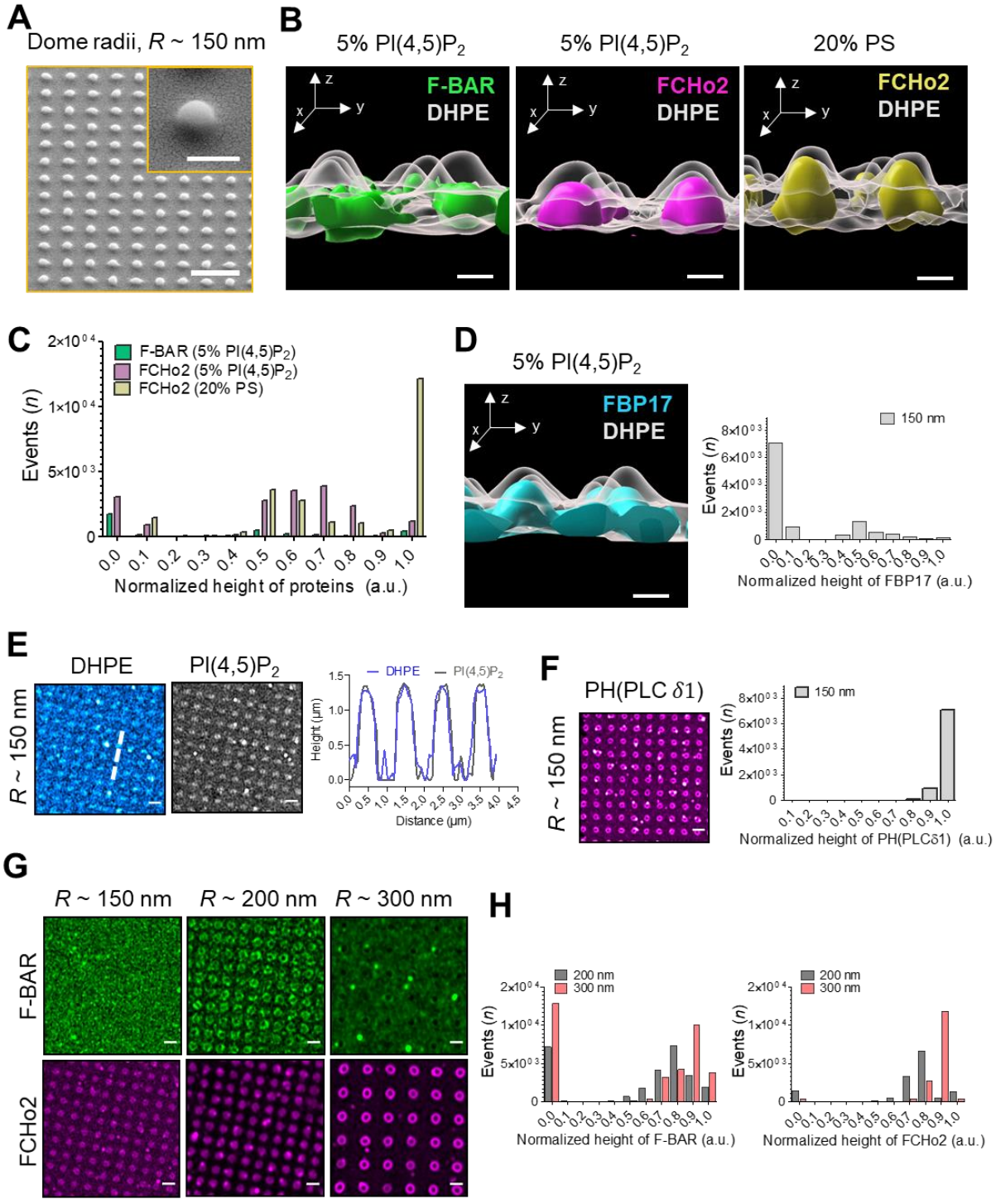
A
Dome radii, R ~ 150 nm
B
5% PI(4,5)P2
5% PI(4,5)P2
20% PS
F-BAR
DHPE
FCHo2
DHPE
FCHo2
DHPE
C
F-BAR (5% PI(4,5)P2)
FCHo2 (5% PI(4,5)P2)
FCHo2 (20% PS)
Events (n)
Normalized height of proteins (a.u.)
D
5% PI(4,5)P2
FBP17
DHPE
150 nm
Events (n)
Normalized height of FBP17 (a.u.)
E
DHPE
PI(4,5)P2
R ~ 150 nm
DHPE
PI(4,5)P2
Height (μm)
Distance (μm)
F
PH(PLC δ1)
R ~ 150 nm
150 nm
Events (n)
Normalized height of PH(PLCδ1) (a.u.)
G
R ~ 150 nm
R ~ 200 nm
R ~ 300 nm
F-BAR
FCHo2
H
200 nm
300 nm
Events (n)
Normalized height of F-BAR (a.u.)
200 nm
300 nm
Events (n)
Normalized height of FCHo2 (a.u.)

Figure 5. **Membrane shape modulates the partitioning of FCHo2 on PI(4,5)P2-containing bilayers .** (A) SEM images of SiO_2 substrates displaying an array of nano-domes with a radius, *R* ~ 150 nm generated by soft-NIL. Scale bar, 2 µm. Inset, scale bar is 500 nm. (B) Representative 3D reconstructions of the surface organization of the F-BAR domain (green) and full-length FCHo2 (magenta) on nano-domes functionalized with 5% mol PI(4,5)P_2-containing membranes, and FCHo2 on nano-domes functionalized with 20% mol of PS (yellow) relative to the DHPE lipid dye signal. Scale bar, 400 nm. (C) Distribution of the normalized maximal height of the surface localization of the F-BAR domain (green) and FCHo2 (magenta) on nano-domes functionalized with 5% mol of PI(4,5)P_2 bilayers and FCHo2 (yellow) on nano-domes functionalized with 20% mol of PS bilayers. n=3300, n=18145, n=23043 for the F-BAR domain and FCHo2 at 5% mol of PI(4,5)P_2 and FCHo2 at 20% mol of PS, respectively. (D) *Left*, representative 3D reconstruction of the surface organization of FBP17 (cyan) on nano-domes functionalized with 5% mol PI(4,5)P_2-containing membranes relative to the DHPE lipid dye signal. Scale bar, 400 nm. *Right*, distribution of the normalized maximal height of the surface localization of FBP17 on nano-domes functionalized with 5% mol of PI(4,5)P_2. n=11252. (E) *Left*, z-stack intensity projected airyscan images of the distribution of fluorescent DHPE and PI(4,5)P_2 on nano-domes of *R* ~ 150 nm. *Right*, cross-section of the normalized maximal height of DHPE (blue) and PI(4,5)P_2 (grey) lipid dyes obtained from the dashed line in the corresponding airyscan image. Scale bar, 2 µm. (F) *Left*, z-stack intensity projected airyscan images of PH (PLCδ1) on nano-domes of *R* ~ 150 nm. Scale bar, 2 µm. *Right*, distribution of the normalized maximal height of the surface localization of PH (PLCδ1) on nano-domes of *R* ~ 150 nm functionalized with 5% mol of PI(4,5)P_2-containing lipid bilayers. n=7974. (G) z-stack intensity projected airyscan images of the distribution of the F-BAR domain (green) and FCHo2 (magenta) on vertical nanostructures of *R* ~ 150 nm, *R* ~ 200 nm and *R* ~ 300 nm functionalized with supported lipid bilayers containing 5% mol of PI(4,5)P_2. Scale bar, 2 µm. (H) Distribution of the normalized maximal height of the surface localization of the F-BAR and FCHo2 on 5% mol of PI(4,5)P_2 lipid functionalized vertical nanostructures of *R* ~ 200 nm and *R* ~ 300 nm. n=26338 and n=34387 for F-BAR and n=13948 and n=15656 for the FCHo2 on structures of *R* ~ 200 nm and *R* ~ 300 nm, respectively.

Discussion

In this study, we report a molecular visualization of the self-assembly of the endocytic protein FCHo2 into ring-like shaped protein patches of several tens of nm on flat PI(4,5)P_2-lipid membranes. Our results point out that the patch formation originates from the diffusion of FCHo2 homodimers via end-to-end interactions, ultimately leading to multiple docking events that contribute to the anisotropic expansion of sub-micrometric molecular clusters. Interestingly, end-to-end interactions were previously described for the F-BAR domain alone, which promoted the assembly of the protein into row-like protein lattices(*11*). Therefore, suggesting that the singular FCHo2 organization that we reported might be required for its biological function. According to *in cellulo* observations, the formation of FCHo2 rings is predicted to be a key feature for the initiation of endocytosis(*6*, *31*). Importantly, we provide the first evidence that, in the absence of other accessory proteins, FCHo2 itself is able to support a ring-like structural organization on flat membranes. Our observations show that the ring formation process expands over ~ 100 s, which is compatible with clathrin-coated vesicles formation(*5*). Moreover, this temporal scale is further maintained during the outgrowth of FCHo2 molecular clusters. Although we observed that addition of cytosolic extracts

promotes FCHo2 reorganization into protein aggregates on *in vitro* membranes, we cannot exclude that on cellular membranes the expansion of the molecular cluster might not participate in the formation of productive clathrin coated pits, which display a typical mean size of ~ 100 nm(*32*). In line with our HS-AFM observations, FCHo2 partitioning at the contour of nano-dome shaped lipid bilayers confirmed that local FCHo2 accumulation on membranes is a diffusion-driven process that appeared to be PI(4,5)P_2-dependent (Figure 5B-C), as membrane curvature and enhanced association rates (Kon/Koff) with PI(4,5)P_2 lipids are reported to affect protein mobility(*14*, *28*). In addition, the different surface localization of the F-BAR domain on vertical nanostructures as compared to the full-length protein points out that the association of FCHo2 with curved membranes might not be exclusively dictated by a scaffolding mechanism (Figure 5), as also reported in the case of FBP17(*33*).

The observation that FCHo2 binds and forms molecular clusters on negatively-charged flat membranes with increased % mol of PI(4,5)P2 supports the model that FCHo2 accumulation on membranes is primarily driven by multivalent interactions and enhanced by the presence of PI(4,5)P_2 (Figure 1), possibly as a result of the multiple binding sites for PS in the F-BAR domain(*22*) and the existence of the PI(4,5)P_2-binding domain(*8*). In spite of the different spatial resolution of sub-diffracted microscopies (such as airyscan, ~100 nm) as compared to HS-AFM (~1 nm), the use of fluorescent lipid dyes allowed us to pinpoint local PI(4,5)P_2 heterogeneities along with FCHo2 clusters within *in vitro* lipid membranes (Figure 1A). Thus, the positive correlation between FCHo2 cluster formation and the presence of PI(4,5)P_2-enriched domains that we found in our study (Figure 1), points out to an organizing role of local phosphoinositide clusters by assisting the recruitment of PI(4,5)P_2-interacting proteins at specific regions of the plasma membrane, as reported for other cellular proteins(*34*, *35*). This preferential localization would also explain the increased FCHo2 structure life-time that we detected on PI(4,5)P_2-enriched domains, as an enhanced electrostatic interaction between the sequestered PI(4,5)P_2 molecules beneath the positively charged surface of the FCHo2 is likely to affect protein dynamics(*14*).

Our experimental observations are in agreement with theoretical and *in cellulo* studies that have shown the association of the EGFR with PI(4,5)P_2(*20*, *21*). The fact that FCHo2 preferentially accumulates on PI(4,5)P_2-enriched domains, as shown in Figure 1, would explain the concomitant detection of FCHo2 and the cargo receptor at the same regions of the cell membrane (Figure 4). As reported by *in cellulo* studies, FCHo1/2 C-terminal μHD domain binds to both cargo and an early complex of scaffolding and adaptor proteins, which also hold cargo-recognition domains, as in the case of Eps15 and AP2 (*8*, *9*, *26*, *36*). In the presence of cytosolic extracts, the local separation of the FCHo2 protein layer into aggregates led to a 1.5-fold increase in the size of FCHo2 molecular clusters (Figure 3), possibly indicating a positive feedback in the accumulation of the protein and/or the reorganization of the cluster due to the presence of FCHo2-

interacting proteins. Because PI(4,5)P_2 is a central hub of the network of proteins early arriving at endocytic sites(*13*, *37*, *38*), we wonder if FCHo2 was able to engage a PI(4,5)P_2 demixing on membranes, as in the case of F-BAR domain of Syp1(*14*). Our data indicates that co-clustering of FCHo2 with the EGFR, but not TfR, promotes the local accumulation of PI(4,5)P_2 at the vicinity of the cargo receptor (Figure 4), thus pointing out that, in the absence of PI(4,5)P_2-metabolizing enzymes, FCHo2-mediated PI(4,5)P_2 segregation might be receptor-specific.

Conclusions

In conclusion, our study provides a molecular picture of the FCHo2 self-assembly into ring-like structures to be a diffusion-driven process that is enhanced by PI(4,5)P_2. While the existence of PI(4,5)P_2-enriched domains confer an organizing role to recruit FCHo2 at specific regions of the membrane, we found that binding of FCHo2 to the plasma membrane triggers the accumulation of PI(4,5)P_2 at the vicinity of the EGFR. Although the exact role of FCHo2-dependent P(4,5)P_2 accumulation in EGFR endocytosis is yet to be established, this observation could explain previous *in cellulo* and *in vivo* studies in which FCHo1/2 depletion was shown to slow down the progression of cargo-loaded clathrin structures (*9*, *10*, *39*, *40*). Because FCHo2 is among the early proteins that are recruited at endocytic sites, the discovery that FCHo2 drives the formation of rings flanked by membrane invaginations along with PI(4,5)P_2 accumulation is fundamental to better understand how clathrin mediated endocytosis is initiated(*6*).

Materials and Methods

Lipids and reagents

Natural and synthetic phospholipids, including POPC, POPS, Egg-PC, Brain-PS, Brain-PI(4,5)P_2 and fluorescent TopFluor-TMR-PtdIns(4,5)P_2 are from Avanti Polar Lipids, Inc. Oregon green 488-DHPE and Alexa Fluor 647 Maleimide labelling kit are from Invitrogen. Atto647N-DOPE and polyclonal rabbit anti-clathrin heavy chain (dilution 1:100; Cat. Nr. HPA059143) was from Sigma. Monoclonal rabbit anti-EGFR (dilution 1:1000; Cat. Nr. 4267) and polyclonal rabbit anti-phospho-EGFR (Tyr1045) (dilution 1:1000; Cat. Nr. 2237) were from Cell Signaling.

EGFR-GFP and TfR-GFP stable cell lines

pRRL.sin.cPPT.SFFV-EGFP/IRES-puro was kindly provided by C. Goujon (IRIM, CNRS UMR9004, Montpellier, France), the EGFR-GFP vector was a gift from Alexander Sorkin, (Addgene plasmid #32751) and the pBa.TfR.GFP vector was a gift from Gary Banker & Marvin Bentley (Addgene plasmid # 4506). The GFP was replaced by a GFP-delta-ATG using these primers: 5'-gtatatatatGGATCCGTGAGCAAGGGCGAGGAG-3' and 5'-CTCACATTGCCAAAAGACG-3'. GFP-delta-ATG fragment replaced the GFP- fragment in pRRL.sin.cPPT.SFFV-EGFP/IRES-puro using a BamHI-XhoI digestion. EGFR was amplified with these primers: 5'-caaatatttgcggccgcATGCGACCCTCCGGGACG-3' and 5'-gtataccggttgaacctccgccTGCTCCAATAAATTCACTGCTTTGTGG-3' and cloned into pRRL.sin.cPPT.SFFV-EGFP-delta-ATG/IRES-puro using NotI-AgeI to generate a fused EGFR-GFP protein.

Lentiviral vector stocks were obtained by polyethylenimine (PEI) -mediated multiple transfection of 293T cells in 6-well plates with vectors expressing Gag-Pol (8.91), the mini-viral genome (pRRL.sin.cPPT.SFFV-EGFR-GFP/IRES-puro) and the Env glycoprotein of VSV (pMD.G) at a ratio of 1:1:0.5. The culture medium was changed 6 hr post-transfection and lentivectors containing supernatants harvested 48 hr later, filtered and stored at -80°C.

The mini-viral genome (pRRL.sin.cPPT.SFFV-TFR-GFP/IRES-puro) and the corresponding lentivectors were generated as detailed in the case of the EGFR-GFP.

To generate a stable cell line HT1080 expressing EGFR-GFP or TfR-GFP, HT1080 cells (a gift from N. Arhel, IRIM, CNRS UMR9004, Montpellier, France) were transduced in 6-well plates using the supernatant of one 6-well plates of the lentiviral stock production detailed above. The culture medium was changed 6 hr post-transduction. Puromycin (1µg/ml) was added 48h after transduction. The percentage of GFP-expressing cells was enumerated by flow cytometry 72 hr after selection under puromycin.

HT1080 cells constitutively expressing the EGFR-GFP or TfR-GFP were cultured in DMEM GlutaMAX supplemented with 10% fetal calf serum, 100 $U \cdot mL^{-1}$ of penicillin and streptomycin and 1$\mu g \cdot ml^{-1}$ of puromycin at 37ºC in 5%CO_2. Cell lines were tested negative for mycoplasma.

Protein purification and protein labeling

pGEX-6P-1 vector coding for the mouse full-length FCHo2 (aa 1-809) and F-BAR domain (aa 1-262) and human FBP17 (aa 1-592) were obtained from H.T McMahon (MRC Laboratory of Molecular Biology, Cambridge, UK). Proteins were subcloned into a pET28a vector with a PreScission protease cleaving site. Proteins were expressed in Rosetta 2 bacteria and purified by affinity chromatography using a HiTrap™ chelating column (GE Healthcare) according to the manufacturer's instructions in 50 mM Tris at pH 8.0, 100 mM NaCl. Proteins were expressed overnight at 18°C using 1 mM IPTG. Proteins were then dialyzed overnight in a Slide-A-Lyzer dialysis cassette (MWCO 10,000) before Alexa Fluor 647 maleimide labelling following the protocol described by the manufacturer (Invitrogen). Protein concentrations were measured using a Bradford assay (Biorad).

Recombinant GST-eGFP-PH-domain (PLCδ1) detecting PI(4,5)P_2 was purified as described in(*29*).

***Xenopus laevis* egg extracts**

Laid eggs are rinsed twice in XB Buffer (100mM KCl, 1mM MgCl2, 0.1mM CaCl2, 50mM sucrose and 10mM HEPES at pH 7.7) and subsequently dejellied with 2% cysteine solution pH7.8. Once dejellied they are extensively rinsed with XB buffer to completely eliminate cysteine solution.

Eggs are then recovered from a Petri dish and treated with Ca2+ Ionophore (final concentration 2 µg/ml) and 35 minutes later, they are crushed by centrifugation for 20min at 10,000g at 4°C. The cytoplasmic layer is collected and supplemented with Cytochalasin B (50ug/ml) Aprotinin (5ug/ml), Leupeptin (5ug/ml) and 10 mM Creatin Phosphate. Cytoplasmic extract is centrifuged again for 20 min at 10,000g. Extract are frozen and then used as described in Figure 3.

Supported lipid bilayers

Lipid mixtures consisted of: 80-85% Egg-PC, 10-15% Brain-PS and 5-10% of Brain-PI(4,5)P_2. The amount of total negatively charged lipids was kept to 20% for any of the mixtures containing phosphoinositides at the expenses of Brain-PS. If needed, fluorescent lipids were added to 0.2%.

For fluorescence microscopy experiments, supported lipid bilayers were prepared as described in(*41*). Experiments were performed by injecting 15 µL of buffer (20 mM Tris, pH 7.4, 150 mM NaCl and 0.5 $mg \cdot ml^{-1}$ of casein). Supported lipid bilayers were imaged on a Zeiss LSM880 confocal microscope.

For HS-AFM experiments, supported lipid bilayers were prepared following the method described in(*42*). Briefly, large unilamellar vesicles (LUVs, diameter ~ 100 nm) were obtained by extrusion of multilamellar vesicles of 85% POPC, 10% POPS and 5% Brain-PI(4,5)P_2 in 20 mM Hepes, pH 7.4, 150 mM NaCl. LUVs

were supplemented with 20 mM of $CaCl_2$ and deposited onto freshly cleaved mica disks. Samples were incubated for 20 min at 60 °C and extensively rinsed with 20 mM Hepes, pH 7.4, 150 mM NaCl, 20 mM EDTA. Finally, bilayers were rinsed and keep under the imaging buffer, 20 mM Hepes, pH 7.4, 150 mM NaCl.

Plasma membrane sheets

Unroofing of HT1080 cells stably expressing the EGFR-GFP was performed by tip sonication as reported in(*43*). Cells were rinsed three times in cold Ringer buffer supplemented with Ca^{2+} (155mM NaCl, 3 mM KCl, 3mM $NaH2PO_4$, 5mM HEPES, 10mM glucose, 2 mM $CaCl_2$, 1mM $MgCl_2$, pH 7.2), then immersed 10 s in Ca^{2+}-free Ringer buffer containing 0.5 mg·mL^{-1} poly-L-lysine. Cells were unroofed by scanning the coverslip with the tip sonicator at 10% of power under HKMgE buffer consisting of 70 mM KCl, 30mM HEPES, 5 mM $MgCl_2$, 3mM EGTA, pH 7.2. Unroofed cells were kept in HKMgE buffer. Fluorescent labeling of plasma membrane sheets was performed immediately after unroofing by incubating the sample with 100 nmol of TopFluor-TMR-PtdIns(4,5)P_2 suspended in 0.2% of absolute ethanol during 5 min, as reported in(*44*). Then, samples were extensively rinsed with HKMgE buffer and immediately imaged under the Zeiss LSM880 confocal microscope. Before addition of 1 µM of FCHo2-Alexa647, unroofed cells were rinsed with HKMgE buffer supplemented with 0.5 mg·ml^{-1} of casein.

Immunofluorescence

Supported lipid bilayers were fixed in 3.7% PFA in PBS for 2 min at room temperature, then rinsed in PBS twice. Samples were stained for the primary antibody for 45 min at room temperature in 1% BSA. Then, the secondary antibody was incubated for 45 min. Finally, samples were extensively rinsed in PBS, then in sterile water and mounted with a Mowiol® 4-88 mounting medium (Polysciences, Inc.). Montage was allowed to solidify in the dark for 48h before microscope acquisitions.

Silica thin film nanostructuration

SiO_2 vertical nanostructures were prepared on conventional borosilicate coverslips with precision thickness No. 1.5 (0.170 ± 0.005 mm), as previously reported(*29*, *45*). Briefly, Si masters were elaborated using LIL Lithography as detailed in(*45*, *46*). PDMS (polydimethylsiloxane) reactants (90 w% RTV141A; 10 w% RTV141B from BLUESIL) were transferred onto the master and dried at 70 °C for 1 h before unmolding.

Silica precursor solution was prepared by adding 4.22 g tetraethyl orthosilicate (TEOS) into 23.26 g absolute ethanol, then 1.5 g HCl (37%), and stirring the solution for 18 h. The final molar composition was

TEOS:HCl:EtOH=1:0.7:25. All the chemicals were from Sigma. Gel films were obtained by dip-coating the coverslips with a ND-DC300 dip-coater (Nadetech Innovations) equipped with an EBC10 Miniclima device to control the surrounding temperature and relative humidity to 20ºC and 45-50%, respectively. The thickness of film was controlled by the withdrawal rate at 300 mm/min. After dip-coating, gel films were consolidated at 430ºC for 5 min. Then, a new layer of the same solution was deposited under the same conditions for printing with the PDMS mold. After imprinting, the samples were transferred to a 70 °C oven for 1 min and then to a 140 °C for 2 min to consolidate the xerogel films before peeling off the PDMS mold. Finally, the sol–gel replicas were annealed at 430 °C for 10 min for consolidation.

Fluorescence microscopy

Images were acquired on a Zeiss LSM880 Airyscan confocal microscope (MRI facility, Montpellier). Excitation sources used were: 405 nm diode laser, an Argon laser for 488 nm and 514 nm and a Helium/Neon laser for 633 nm. Acquisitions were performed on a 63x/1.4 objective. Multidimensional acquisitions were acquired via an Airyscan detector (32-channel GaAsP photomultiplier tube (PMT) array detector). 3D images were acquired by fixing a 0.15 µm z-step in order to cover the entire surface of vertical nanostructures.

HS-AFM imaging

HS-AFM movies were acquired with an HS-AFM (SS-NEX, Research Institute of Biomolecule Metrology, Tsukuba, Japan) equipped with a superluminescent diode (wavelength, 750 nm; EXS 7505-B001, Exalos, Schlieren, Switzerland) and a digital high-speed lock-in Amplifier (Hinstra, Transcommers, Budapest, Hungary)(*47*) following the protocol detailed at(*48*). Scanning was performed using USC-1.2 cantilevers featuring an electron beam deposition tip (NanoWorld, Neuchâtel, Switzerland) with a nominal spring constant k = 0.15 N/m, resonance frequency f(r) = 600 kHz, and quality factor Qc ≈ 2 under liquid conditions. For high-resolution imaging, the electron beam deposition tip was sharpened by helium plasma etching using a plasma cleaner (Diener Electronic, Ebhausen, Germany). Images were acquired in amplitude modulation mode at the minimal possible applied force that enables good quality of imaging under optical feedback parameters.

Image processing and quantification

Line profiles of the fluorescence intensities were done using ImageJ(*49*) and the kymographs were made using the Kymograph plugin (http://www.embl.de/eamnet/html/body_kymograph.html).

Protein binding was quantified by measuring the mean grey value of the protein channel that was then normalized by the mean gray value of the membrane intensity (as indicated by the TF-TMR-PI(4,5)P_2 fluorescence) in the same image. Mean gray values were measured once protein binding reached the steady-state, which was estimated from the binding kinetics to be < 4 min. Protein binding was averaged from N > 3 experimental replicates. Mean gray values were measured using ImageJ. Concentrations and confocal parameters were kept constant between experiments and samples.

The automatic analysis of images to determine molecular clusters was performed with ImageJ(*49*). Spots of different sizes are detected using a scale space spot detection (*50*) and overlapping spots are merged. The LoG filter of the FeatureJ plugin(*51*) is used to create the scale space. Starting points are detected as local minima of the minimum projection and as minima on the smallest scale. A simplified linking scheme is applied that looks for minima along the scales for each starting point within the radius of the spot on the given scale. Two spots are merged if at least 20 percent of the surface of one spot is covered by the other. The noise tolerance for the spot detection is determined manually for each series of input images.

To determine the height of each protein surface on SiO_2 vertical nanostructures, we applied an automated image analysis procedure that calculates the statistics about the average maximal height of the signal in each channel of interest, as previously described(*29*). The analysis has been implemented as an ImageJ(*49*) macro toolset(*52*).

HS-AFM images were processed using Gwyddion, an open-source software for SPM data analysis, and WSxM(*53*).

Data representation and statistical analysis

Representation of cross-section analysis and recruitment curves was performed using Origin software.

3D rendering of Airyscan images was generated with the 3/4D visualization and analysis software Imaris (Oxford Instruments).

Statistical analysis was performed using Prism GraphPad software.

References

1. G. Di Paolo, P. De Camilli, Phosphoinositides in cell regulation and membrane dynamics. *Nature*. **443**, 651–657 (2006).

2. M. A. D. Matteis, A. Godi, PI-loting membrane traffic. *Nat Cell Biol*. **6**, 487–492 (2004).

3. Y. Posor, M. Eichhorn-Gruenig, D. Puchkov, J. Schöneberg, A. Ullrich, A. Lampe, R. Müller, S. Zarbakhsh, F. Gulluni, E. Hirsch, M. Krauss, C. Schultz, J. Schmoranzer, F. Noé, V. Haucke, Spatiotemporal control of endocytosis by phosphatidylinositol-3,4-bisphosphate. *Nature*. **499**, 233–237 (2013).

4. Y. Posor, M. Eichhorn-Grünig, V. Haucke, Phosphoinositides in endocytosis. *Biochimica et Biophysica Acta (BBA) - Molecular and Cell Biology of Lipids*. **1851**, 794–804 (2015).

5. M. J. Taylor, D. Perrais, C. J. Merrifield, A High Precision Survey of the Molecular Dynamics of Mammalian Clathrin-Mediated Endocytosis. *PLoS Biol*. **9**, e1000604 (2011).

6. V. Haucke, M. M. Kozlov, Membrane remodeling in clathrin-mediated endocytosis. *J Cell Sci*. **131**, jcs216812 (2018).

7. C. Godlee, M. Kaksonen, From uncertain beginnings: Initiation mechanisms of clathrin-mediated endocytosis. *J Cell Biol*. **203**, 717–725 (2013).

8. W. M. Henne, E. Boucrot, M. Meinecke, E. Evergren, Y. Vallis, R. Mittal, H. T. McMahon, FCHo Proteins Are Nucleators of Clathrin-Mediated Endocytosis. *Science*. **328**, 1281–1284 (2010).

9. L. Ma, P. K. Umasankar, A. G. Wrobel, A. Lymar, A. J. McCoy, S. S. Holkar, A. Jha, T. Pradhan-Sundd, S. C. Watkins, D. J. Owen, L. M. Traub, Transient Fcho1/2·Eps15/R·AP-2 Nanoclusters Prime the AP-2 Clathrin Adaptor for Cargo Binding. *Developmental Cell*. **37**, 428–443 (2016).

10. G. Hollopeter, J. J. Lange, Y. Zhang, T. N. Vu, M. Gu, M. Ailion, E. J. Lambie, B. D. Slaughter, J. R. Unruh, L. Florens, E. M. Jorgensen, The membrane-associated proteins FCHo and SGIP are allosteric activators of the AP2 clathrin adaptor complex. *eLife*. **3**, e03648 (2014).

11. A. Frost, R. Perera, A. Roux, K. Spasov, O. Destaing, E. H. Egelman, P. De Camilli, V. M. Unger, Structural Basis of Membrane Invagination by F-BAR Domains. *Cell*. **132**, 807–817 (2008).

12. W. M. Henne, H. M. Kent, M. G. J. Ford, B. G. Hegde, O. Daumke, P. J. G. Butler, R. Mittal, R. Langen, P. R. Evans, H. T. McMahon, Structure and Analysis of FCHo2 F-BAR Domain: A Dimerizing and Membrane Recruitment Module that Effects Membrane Curvature. *Structure*. **15**, 839–852 (2007).

13. R. Zoncu, R. M. Perera, R. Sebastian, F. Nakatsu, H. Chen, T. Balla, G. Ayala, D. Toomre, P. V. De Camilli, Loss of endocytic clathrin-coated pits upon acute depletion of phosphatidylinositol 4,5-bisphosphate. *Proceedings of the National Academy of Sciences*. **104**, 3793–3798 (2007).

14. H. Zhao, A. Michelot, E. V. Koskela, V. Tkach, D. Stamou, D. G. Drubin, P. Lappalainen, Membrane-Sculpting BAR Domains Generate Stable Lipid Microdomains. *Cell Reports*. **4**, 1213–1223 (2013).

15. L. Picas, J. Viaud, K. Schauer, S. Vanni, K. Hnia, V. Fraisier, A. Roux, P. Bassereau, F. Gaits-Iacovoni, B. Payrastre, J. Laporte, J.-B. Manneville, B. Goud, BIN1/M-Amphiphysin2 induces clustering of phosphoinositides to recruit its downstream partner dynamin. *Nat Commun*. **5**, 5647 (2014).

16. M. Krauss, V. Kukhtina, A. Pechstein, V. Haucke, Stimulation of phosphatidylinositol kinase type I-mediated phosphatidylinositol (4,5)-bisphosphate synthesis by AP-2 -cargo complexes. *Proceedings of the National Academy of Sciences*. **103**, 11934–11939 (2006).

17. Z. Kadlecova, S. J. Spielman, D. Loerke, A. Mohanakrishnan, D. K. Reed, S. L. Schmid, Regulation of clathrin-mediated endocytosis by hierarchical allosteric activation of AP2. *Journal of Cell Biology*. **216**, 167–179 (2017).

18. S. Höning, D. Ricotta, M. Krauss, K. Späte, B. Spolaore, A. Motley, M. Robinson, C. Robinson, V. Haucke, D. J. Owen, Phosphatidylinositol-(4,5)-Bisphosphate Regulates Sorting Signal Recognition by the Clathrin-Associated Adaptor Complex AP2. *Molecular Cell*. **18**, 519–531 (2005).

19. H. Koldsø, D. Shorthouse, J. Hélie, M. S. P. Sansom, Lipid Clustering Correlates with Membrane Curvature as Revealed by Molecular Simulations of Complex Lipid Bilayers. *PLoS Comput Biol*. **10**, e1003911 (2014).

20. K. B. Abd Halim, H. Koldsø, M. S. P. Sansom, Interactions of the EGFR juxtamembrane domain with PIP2-containing lipid bilayers: Insights from multiscale molecular dynamics simulations. *Biochimica et Biophysica Acta (BBA) - General Subjects*. **1850**, 1017–1025 (2015).

21. Y. Wang, J. Gao, X. Guo, T. Tong, X. Shi, L. Li, M. Qi, Y. Wang, M. Cai, J. Jiang, C. Xu, H. Ji, H. Wang, Regulation of EGFR nanocluster formation by ionic protein-lipid interaction. *Cell Res*. **24**, 959–976 (2014).

22. T. Itoh, K. S. Erdmann, A. Roux, B. Habermann, H. Werner, P. De Camilli, Dynamin and the Actin Cytoskeleton Cooperatively Regulate Plasma Membrane Invagination by BAR and F-BAR Proteins. *Developmental Cell*. **9**, 791–804 (2005).

23. A. Walrant, D. S. Saxton, G. P. Correia, J. L. Gallop, in *Methods in Cell Biology* (Elsevier, 2015; https://linkinghub.elsevier.com/retrieve/pii/S0091679X1500062X), vol. 128, pp. 125–147.

24. F. Daste, A. Walrant, M. R. Holst, J. R. Gadsby, J. Mason, J.-E. Lee, D. Brook, M. Mettlen, E. Larsson, S. F. Lee, R. Lundmark, J. L. Gallop, Control of actin polymerization via the coincidence of phosphoinositides and high membrane curvature. *J. Cell Biol*. **216**, 3745–3765 (2017).

25. M. Wu, B. Huang, M. Graham, A. Raimondi, J. E. Heuser, X. Zhuang, P. De Camilli, Coupling between clathrin-dependent endocytic budding and F-BAR-dependent tubulation in a cell-free system. *Nat Cell Biol*. **12**, 902–908 (2010).

26. A. Reider, S. L. Barker, S. K. Mishra, Y. J. Im, L. Maldonado-Báez, J. H. Hurley, L. M. Traub, B. Wendland, Syp1 is a conserved endocytic adaptor that contains domains involved in cargo selection and membrane tubulation. *EMBO J*. **28**, 3103–3116 (2009).

27. A. Arkhipov, Y. Shan, R. Das, N. F. Endres, M. P. Eastwood, D. E. Wemmer, J. Kuriyan, D. E. Shaw, Architecture and Membrane Interactions of the EGF Receptor. *Cell*. **152**, 557–569 (2013).

28. Y. A. Domanov, S. Aimon, G. E. S. Toombes, M. Renner, F. Quemeneur, A. Triller, M. S. Turner, P. Bassereau, Mobility in geometrically confined membranes. *Proceedings of the National Academy of Sciences*. **108**, 12605–12610 (2011).

29. T. Sansen, D. Sanchez-Fuentes, R. Rathar, A. Colom-Diego, F. El Alaoui, J. Viaud, M. Macchione, S. de Rossi, S. Matile, R. Gaudin, V. Bäcker, A. Carretero-Genevrier, L. Picas, *ACS Appl. Mater. Interfaces*, in press, doi:10.1021/acsami.0c05432.

30. B. Qualmann, D. Koch, M. M. Kessels, Let's go bananas: revisiting the endocytic BAR code. *EMBO J*. **30**, 3501–3515 (2011).

31. K. A. Sochacki, A. M. Dickey, M.-P. Strub, J. W. Taraska, Endocytic proteins are partitioned at the edge of the clathrin lattice in mammalian cells. *Nat Cell Biol*. **19**, 352–361 (2017).

32. H. T. McMahon, E. Boucrot, Molecular mechanism and physiological functions of clathrin-mediated endocytosis. *Nat Rev Mol Cell Biol*. **12**, 517–533 (2011).

33. Comparative Study of Curvature Sensing Mediated by F-BAR and an Intrinsically Disordered Region of FBP17 | Elsevier Enhanced Reader, , doi:10.1016/j.isci.2020.101712.

34. A. Honigmann, G. van den Bogaart, E. Iraheta, H. J. Risselada, D. Milovanovic, V. Mueller, S. Müllar, U. Diederichsen, D. Fasshauer, H. Grubmüller, S. W. Hell, C. Eggeling, K. Kühnel, R. Jahn, Phosphatidylinositol 4,5-bisphosphate clusters act as molecular beacons for vesicle recruitment. *Nat Struct Mol Biol*. **20**, 679–686 (2013).

35. W. D. Heo, T. Inoue, W. S. Park, M. L. Kim, B. O. Park, T. J. Wandless, T. Meyer, PI(3,4,5)P3 and PI(4,5)P2 Lipids Target Proteins with Polybasic Clusters to the Plasma Membrane. *Science*. **314**, 1458–1461 (2006).

36. L. M. Traub, J. S. Bonifacino, Cargo Recognition in Clathrin-Mediated Endocytosis. *Cold Spring Harbor Perspectives in Biology*. **5**, a016790–a016790 (2013).

37. C. N. Antonescu, F. Aguet, G. Danuser, S. L. Schmid, Phosphatidylinositol-(4,5)-bisphosphate regulates clathrin-coated pit initiation, stabilization, and size. *MBoC*. **22**, 2588–2600 (2011).

38. B. T. Kelly, S. C. Graham, N. Liska, P. N. Dannhauser, S. Höning, E. J. Ungewickell, D. J. Owen, AP2 controls clathrin polymerization with a membrane-activated switch, 6.

39. P. K. Umasankar, S. Sanker, J. R. Thieman, S. Chakraborty, B. Wendland, M. Tsang, L. M. Traub, Distinct and separable activities of the endocytic clathrin-coat components Fcho1/2 and AP-2 in developmental patterning. *Nat Cell Biol*. **14**, 488–501 (2012).

40. E. E. Mulkearns, J. A. Cooper, FCH domain only-2 organizes clathrin-coated structures and interacts with Disabled-2 for low-density lipoprotein receptor endocytosis. *MBoC*. **23**, 1330–1342 (2012).

41. J. A. Braunger, C. Kramer, D. Morick, C. Steinem, Solid Supported Membranes Doped with PIP_2: Influence of Ionic Strength and pH on Bilayer Formation and Membrane Organization. *Langmuir*. **29**, 14204–14213 (2013).

42. L. Picas, A. Carretero-Genevrier, M. T. Montero, J. L. Vázquez-Ibar, B. Seantier, P.-E. Milhiet, J. Hernández-Borrell, Preferential insertion of lactose permease in phospholipid domains: AFM observations. *Biochimica et Biophysica Acta (BBA) - Biomembranes*. **1798**, 1014–1019 (2010).

43. J. Heuser, The Production of 'Cell Cortices' for Light and Electron Microscopy. *Traffic*. **1**, 545–552 (2000).

44. V. Mueller, C. Ringemann, A. Honigmann, G. Schwarzmann, R. Medda, M. Leutenegger, S. Polyakova, V. N. Belov, S. W. Hell, C. Eggeling, STED Nanoscopy Reveals Molecular Details of Cholesterol- and Cytoskeleton-Modulated Lipid Interactions in Living Cells. *Biophysical Journal*. **101**, 1651–1660 (2011).

45. Q. Zhang, D. Sánchez-Fuentes, R. Desgarceaux, P. Escofet-Majoral, J. Oró-soler, J. Gázquez, G. Larrieu, B. Charlot, A. Gómez, M. Gich, A. Carretero-Genevrier, Micro/Nanostructure Engineering of Epitaxial Piezoelectric α-Quartz Thin Films on Silicon. *ACS Appl. Mater. Interfaces*. **12**, 4732–4740 (2020).

46. Q. Zhang, D. Sánchez-Fuentes, A. Gómez, R. Desgarceaux, B. Charlot, J. Gàzquez, A. Carretero-Genevrier, M. Gich, *Nanoscale Adv.*, in press, doi:10.1039/C9NA00388F.

47. A. Colom, I. Casuso, F. Rico, S. Scheuring, A hybrid high-speed atomic force–optical microscope for visualizing single membrane proteins on eukaryotic cells. *Nat Commun*. **4**, 2155 (2013).

48. F. Zuttion, L. Redondo-Morata, A. Marchesi, I. Casuso, in *Nanoscale Imaging: Methods and Protocols*, Y. L. Lyubchenko, Ed. (Springer, New York, NY, 2018; https://doi.org/10.1007/978-1-4939-8591-3_11), *Methods in Molecular Biology*, pp. 181–200.

49. C. A. Schneider, W. S. Rasband, K. W. Eliceiri, NIH Image to ImageJ: 25 years of image analysis. *Nat Methods*. **9**, 671–675 (2012).

50. T. Lindeberg, *Scale-Space Theory in Computer Vision* (Springer US, 1994; https://www.springer.com/gp/book/9780792394181), *The Springer International Series in Engineering and Computer Science*.

51. FeatureJ, (available at https://imagescience.org/meijering/software/featurej/).

52. https://github.com/MontpellierRessourcesImagerie/imagej_macros_and_scripts/wiki/MRI_Heights_of_Surfaces_Tools.

53. I. Horcas, R. Fernández, J. M. Gómez-Rodríguez, J. Colchero, J. Gómez-Herrero, A. M. Baro, WSXM: A software for scanning probe microscopy and a tool for nanotechnology. *Review of Scientific Instruments*. **78**, 013705 (2007).

Acknowledgements

The authors thank H.T. McMahon for kindly providing F-BAR domain protein constructs. C. Goujon and O. Moncorgé for helping in the transduction of HT1080 cells. C. Holuka for assistance with plasma membrane sheets. P. Maiuri for assistance in data analysis. S. Roche, C. Favard, and D. Muriaux for scientific discussions. We acknowledge the imaging facility MRI, member of the national infrastructure France-BioImaging infrastructure supported by the French National Research Agency (ANR-10-INBS-04, «Investments for the future»). L.P. acknowledges the ATIP-Avenir program (AO-2016) and ANR-18-CE13-0015-02 for financial support. A.C-G. acknowledges the financial support from the European Research Council (ERC) under the European Union's Horizon 2020 research and innovation program (No.803004).

Author contributions

F.E-A and L.P conceptualized the study. F.E-A. I.C., D.S-F, R.R., A.C-G and L.P. performed experiments and/or analyzed results. F.E-A. and J.V. generated the recombinant proteins used in this study. T.L. and A.C. produced the *X. laevis* egg extracts. S.V participated in the production of plasma membrane sheets. V.B. designed the automated analysis of images. C.A-A. generated the HT1080 stable cell lines. F.E-A and L.P wrote the manuscript. All authors contributed to the last version of the manuscript.

Supporting information

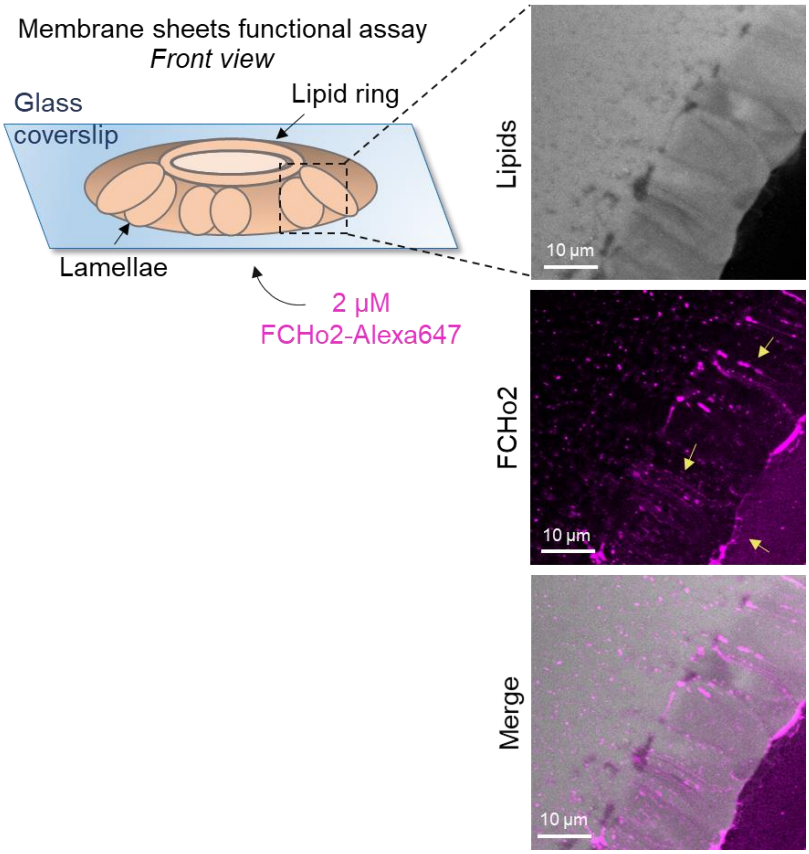

Figure S1. *Left*, schematic representation of the membrane sheets *in vitro* assay, as detailed by Itoh *et al*.(*22*), to test the functionality of recombinant full-length FCHo2-Alexa647. Membrane sheets were made using brain polar lipid extracts (Avanti). *Right*, representative still confocal images showing the formation of membrane tubes after addition of 2 µM of FCHo2, as indicated by yellow arrows.

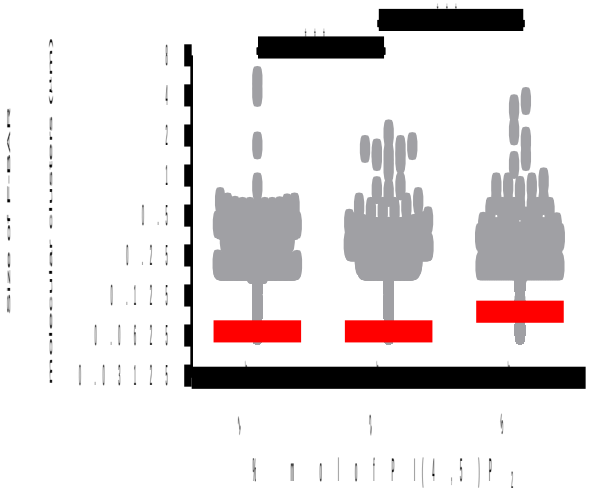

Figure S2. Comparison of the size of molecular clusters of the F-BAR domain as a function of the % mol of PI(4,5)P_2.

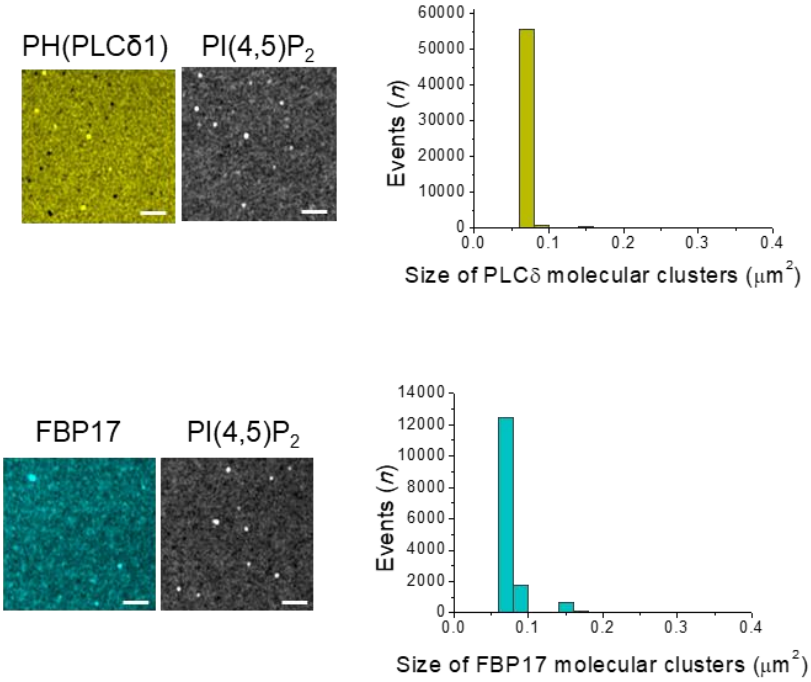

Figure S3. Organization and distribution of the size of the spots of PLCδ1 (top) and FBP17 (bottom) on supported lipid bilayers containing 5 % mol of PI(4,5)P_2.

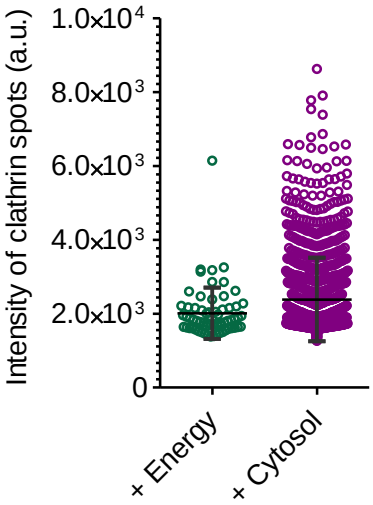

Figure S4. Intensity and number of clathrin spots detected with a mouse anti-clathrin antibody/anti-mouse Alexa488 antibody on 5% mol PI(4,5)P_2-containing membranes incubated with the energy mix alone or with 4 mg/ml of cytosolic extract.

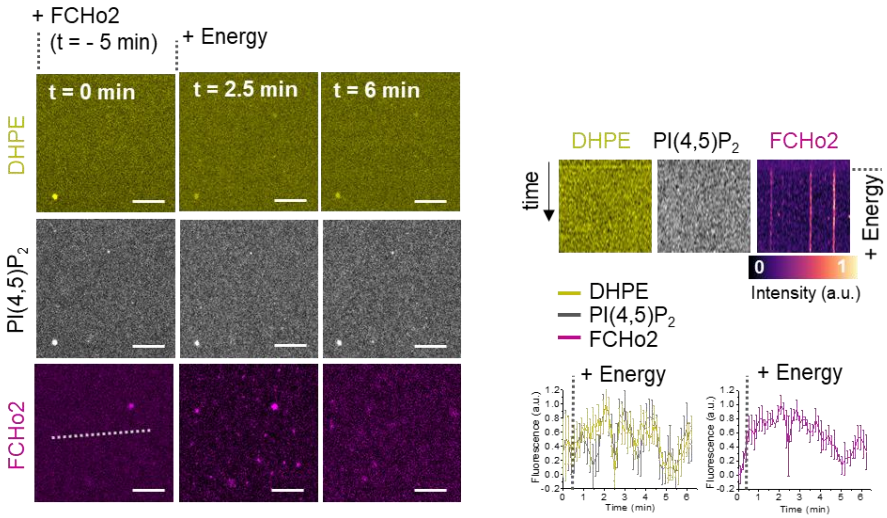

Figure S5. *Left*, airyscan time-lapse showing the membrane reorganization of DHPE (yellow), PI(4,5)P_2 (grey) and FCHo2 (magenta) after injection of the energy mix (+ Energy). *Top right*, kymograph analysis along the dashed line. Time scale is 6 min. Scale bar, 5 µm. *Bottom right*, fluorescence quantification over time of DHPE (yellow), PI(4,5)P_2 (grey) and FCHo2 (magenta) upon addition of the energy mix (+ Energy). Each curve represents the mean ± s.d., n = 7.

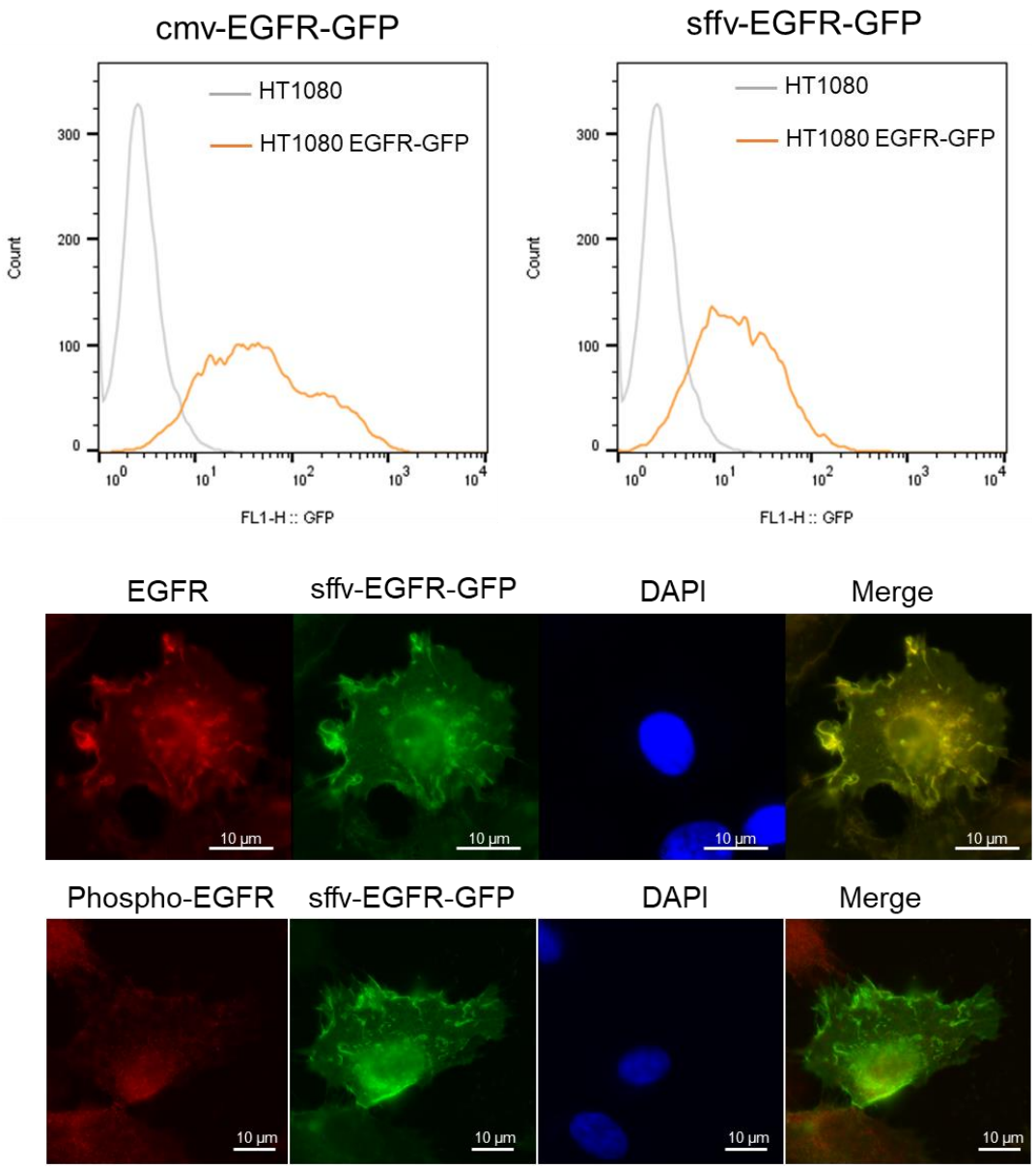

Figure S6. Characterization of the EGFR-GFP expression and EGFR phosphorylation (phospho-EGFR, Polyclonal rabbit anti-phospho-EGF receptor (Tyr1045) Antibody (Cat. No. 2237, Cell Signaling) on transduced HT1080 cells.

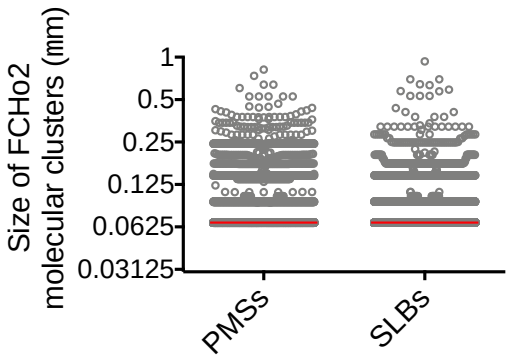

Figure S7. Comparison of the size distribution of FCHo2 molecular clusters obtained on EGFR-GFP plasma membrane sheets (PMSs) 5% mole PI(4,5)P_2-containing supported lipid bilayers (SLBs).

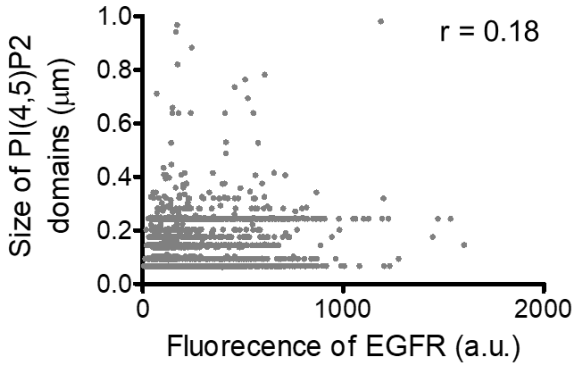

Figure S8. Correlation between the size of PI(4,5)P_2-enriched domains and the fluorescence intensity of the EGFR-GFP on plasma membrane sheets. The correlation coefficient, r, is displayed in the figure.

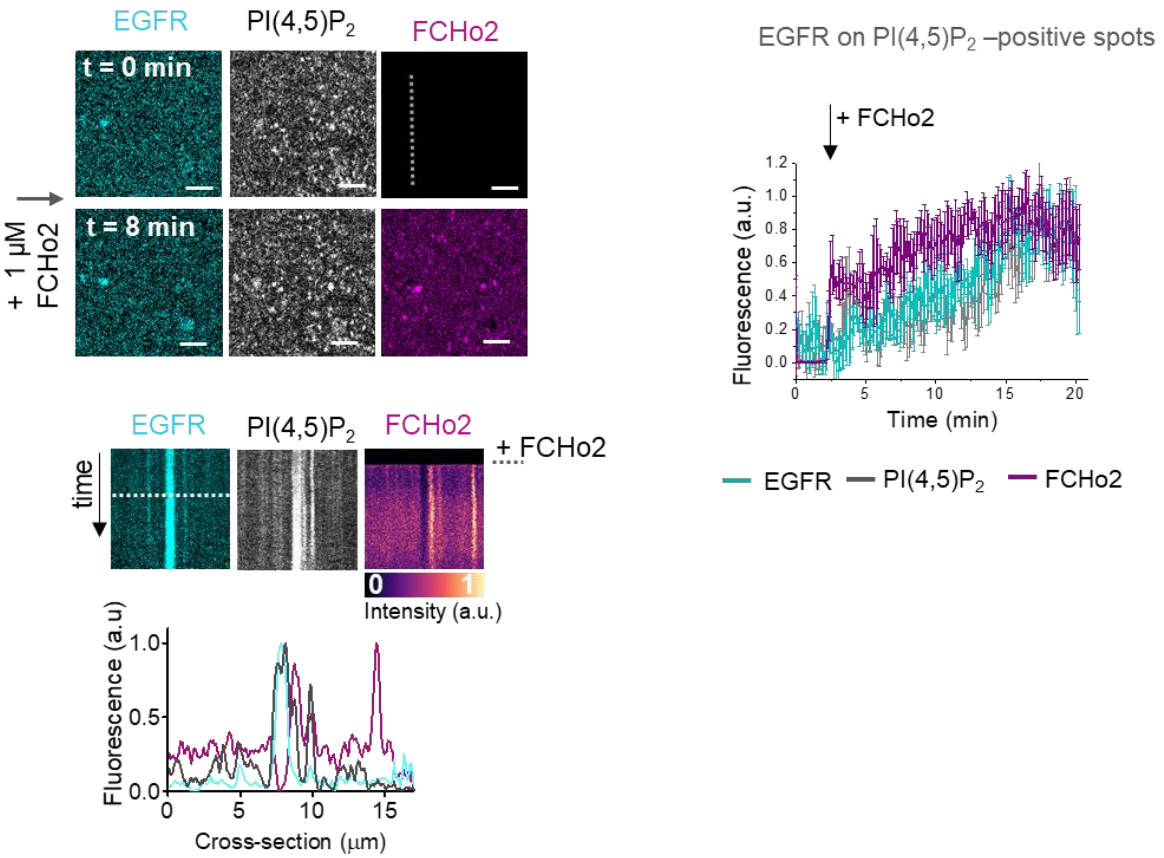

Figure S9. Recruitment of FCHo2 on EGFR and PI(4,5)P_2-positive spots on EGFR-GFP plasma membrane sheets.

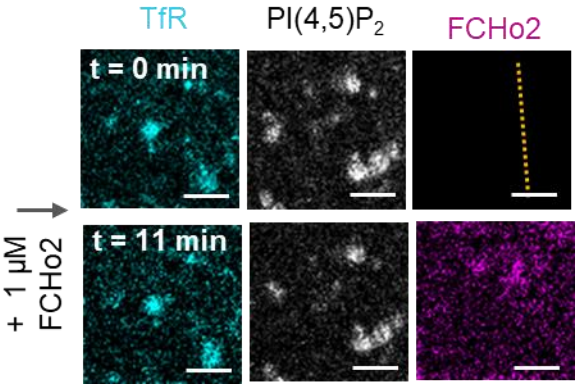

Figure S10. Recruitment of FCHo2 on TfR-GFP plasma membrane sheets.

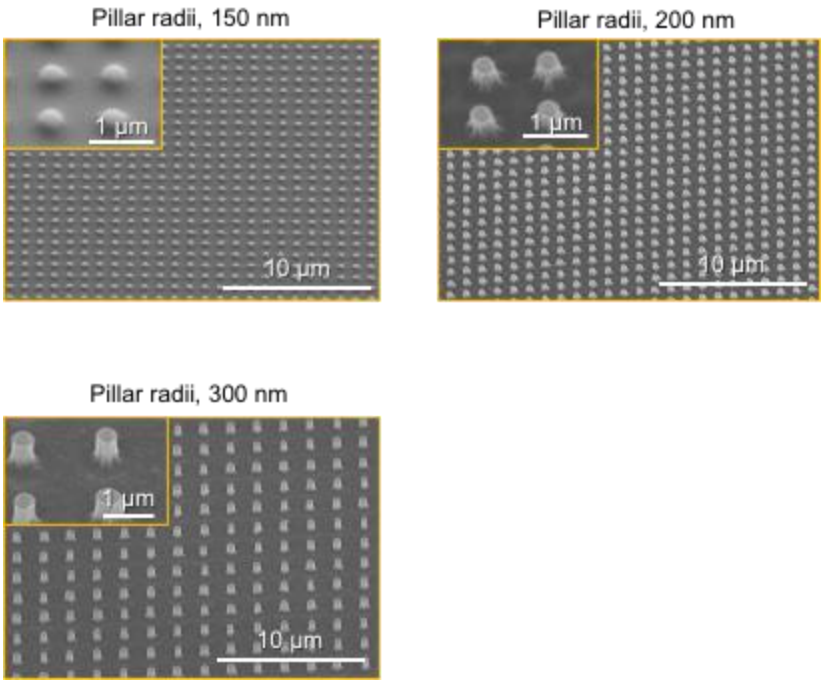

Figure S11. Scanning Electron Microscopy (SEM) images of the different nanostructured substrates that were used to manipulate the shape of supported lipid bilayers.

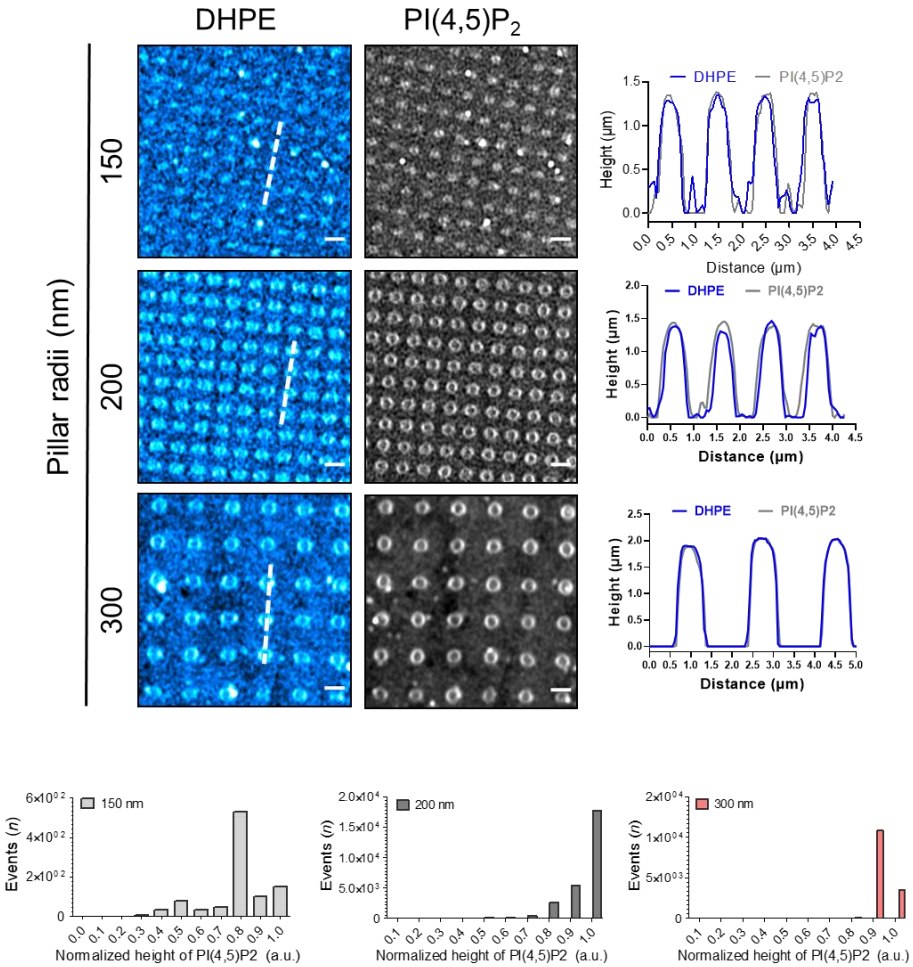

Figure S12. Surface localization of TF-TMR-PI(4,5)P_2 dye respect to OG-DHPE on vertical nanostructures of different radii of curvature.

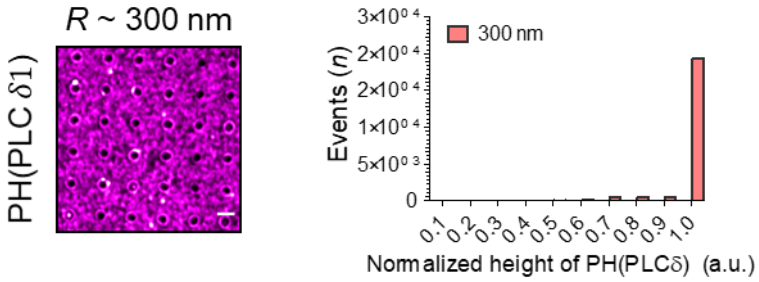

Figure S13. Surface localization of PH(PLCδ1) respect to OG-DHPE dye on vertical nanostructures of radius ~ 300 nm.